Space Sci Rev (2016) 199:407–470
DOI 10.1007/s11214-014-0119-6

Hot Plasma Composition Analyzer for the Magnetospheric Multiscale Mission

D.T. Young · J.L. Burch · R.G. Gomez · A. De Los Santos · G.P. Miller · P. Wilson IV · N. Paschalidis · S.A. Fuselier · K. Pickens · E. Hertzberg · C.J. Pollock · J. Scherrer · P.B. Wood · E.T. Donald · D. Aaron · J. Furman · D. George · R.S. Gurnee · R.S. Hourani · A. Jacques · T. Johnson · T. Orr · K.S. Pan · S. Persyn · S. Pope · J. Roberts · M.R. Stokes · K.J. Trattner · J.M. Webster

Received: 24 March 2014 / Accepted: 6 November 2014 / Published online: 24 December 2014

Abstract This paper describes the science motivation, measurement objectives, performance requirements, detailed design, approach and implementation, and calibration of the four Hot Plasma Composition Analyzers (HPCA) for the Magnetospheric Multiscale mission. The HPCA is based entirely on electrostatic optics combining an electrostatic energy analyzer with a carbon-foil based time-of-flight analyzer. In order to fulfill mission requirements, the HPCA incorporates three unique technologies that give it very wide dynamic range capabilities essential to measuring minor ion species in the presence of extremely high proton fluxes found in the region of magnetopause reconnection. Dynamic range is controlled primarily by a novel radio frequency system analogous to an RF mass spectrometer. The RF, in combination with capabilities for high TOF event processing rates and high current micro-channel plates, ensures the dynamic range and sensitivity needed for accurate measurements of ion fluxes between ∼1 eV and 40 keV that are expected in the region of

D.T. Young (✉) · J.L. Burch · R.G. Gomez · A. De Los Santos · G.P. Miller · P. Wilson IV · S.A. Fuselier · K. Pickens · J. Scherrer · P.B. Wood · D. Aaron · J. Furman · D. George · T. Johnson · T. Orr · K.S. Pan · S. Persyn · S. Pope · J. Roberts · J.M. Webster
Space Science and Engineering Division, Southwest Research Institute, San Antonio, TX 78238, USA
e-mail: dyoung@swri.edu

E. Hertzberg
Lockheed Martin Advanced Technology Center, Palo Alto, CA 94304, USA

E.T. Donald · R.S. Gurnee · R.S. Hourani · M.R. Stokes
Space Exploration Sector, Johns Hopkins University, Applied Physics Laboratory, Laurel, MD 20723, USA

N. Paschalidis · A. Jacques
Code 670, NASA Goddard Space Flight Center, Greenbelt, MD 20771, USA

C.J. Pollock
Code 673, NASA Goddard Space Flight Center, Greenbelt, MD 20771, USA

K.J. Trattner
Laboratory for Atmospheric and Space Physics, University of Colorado, Boulder, CO 80303, USA

reconnection events. A third technology enhances mass resolution in the presence of high proton flux.

In order to calibrate the four HPCA instruments we have developed a unique ion calibration system. The system delivers a multi-species beam resolved to $M/\Delta M \sim 100$ and current densities between 0.05 and 200 pA/cm^2 with a stability of ± 5 %. The entire system is controlled by a dedicated computer synchronized with the HPCA ground support equipment. This approach results not only in accurate calibration but also in a comprehensive set of coordinated instrument and auxiliary data that makes analysis straightforward and ensures archival of all relevant data.

Keywords Plasma ion composition · Reconnection measurements · Time-of-Flight mass spectrometry

Glossary

ASIC	Application specific integrated circuit
CAPS	Cassini Plasma Spectrometer
C&DH	Command and data handling
CCSDS	Consultative Committee for Space Data Systems (a telemetry standard)
CFD	Constant fraction discriminator
CIDP	Central Instrument Data Processor
CRU	Calibration Reference Unit
DAC	Digital-to-analog converter
DIS	Dual Ion Sensors
EEPROM	Electrically Erasable Programmable Read-Only Memory
EGSE	Electrical Ground Support Equipment
EPD	Energetic Particle Detector
EPIC	Energetic Plasma Ion Calibration system
ESA	Electrostatic analyzer
FC	Faraday cup
FEE	Front-end electronics
FM	HPCA Flight Model (1 through 4)
FOV	Field-of-view
FPGA	Field programmable gate array
FPI	Fast Plasma Instrument
FSW	Flight software
FWHM	Full-width at half maximum
HPCA	Hot Plasma Composition Analyzer
HV	High voltage
HVPS	High Voltage Power Supply
LVPS	Low Voltage Power Supply
Mbps	Megabits/second
MCP	Microchannel-plate detector
MMS	Magnetospheric Multiscale Mission
PCB	Printed circuit board
Rice	A lossless data compression technique named for Robert F. Rice
RF	Radiofrequency
SNR	Signal-to-noise ratio
SOC	Science Operations Center
SPARC	8-core 1.2 GHz Microprocessor

TIDE	Thermal Ion Detector Experiment
TOF	Time-of-flight
TOFA	Time-of-flight Analyzer
UHV	Ultra-high vacuum

Symbols

A	Instrument aperture area
A_{eff}	Instrument effective area
A_{FC}	Faraday cup aperture area
B	Magnetic field strength
c	Speed of light
c_A	Alfven velocity
$C_{ij}(v)$	Counting rate for species i at energy step j
e	Electron charge
E^*	Total ion energy inside TOF analyzer
E_j	Ion energy at step j
$E/\Delta E$	Energy resolution
ΔE_{foil}	Energy lost in carbon foil due to scattering
E_{max}	Maximum ion energy scanned
E_{min}	Minimum energy scanned
$f_{ij}(v)$	Ion velocity distribution function for species i at energy step j
F_{ij}	Differential directional ion number flux
G_v	Velocity-dependent geometric factor
H	Perpendicular distance from foil center to MCP
i	Species identifier
j	Energy step number
I_0	Calibration ion beam current
k	ESA analyzer constant
k_{ESA}	Calibration reference unit ESA analyzer constant
L	Ion path length from foil to MCP
L_C	Slant distance from a foil center to the MCP center
L_0	Slant distance from the foil normal to the MCP
$\mathcal{M}$	Mach number
M_i	Ion mass/charge for species i
M_p	Proton mass
M/q	Ion mass/charge ratio
$M/\Delta M$	Mass resolution
N	Total ion number density
N_B	Calibration ion beam number density
N'	Number density measured by a non-mass-discriminating electrostatic analyzer
N_i	Number density of ion species i
P_i	Ion pressure
q	Total ion charge
R	Radius on MCP of ion with path length L
R_0	Toroid major radius
R_1	Toroid minor radius
R_{Exit}	Radius of the center of the ESA exit
R_{Foil}	Radius to the center of the carbon foils
R_{MCP}	Radius of the MCP sensitive area

T	Ion time-of-flight
$T/\Delta T$	TOF resolution
$t_{\max}$	Maximum TOF through the TOF flight volume
v	Velocity
V_B	Calibration ion beam velocity
V_j	High voltage applied to ESA at energy step j
V_{acc}	TOF acceleration voltage
V_0	Ion directional flow velocity
v_{th}	Ion thermal velocity
α	Azimuthal angle
β	Elevation angle
$\Delta\alpha$	Azimuthal angle resolution
$\Delta\beta$	Elevation angle resolution
Δ_i	Ion inertial length for species i
Δt	Measurement interval
ΔV_{ESA}	Voltage applied to the CRU ESA
ε_{ij}	Species- and energy-dependent detector efficiency (≤ 1)
ε_0	Permittivity of free space
γ_{ESA}	ESA bending angle
γ	Square root of the ratio of ion mass to proton mass
κ_i	Fractional number density of heavy ions
μ_0	Vacuum permeability
ρ	Ion mass density
ρ'	Mass density measured by a non-mass-discriminating electrostatic analyzer
Φ	Angle between foil normal and plane of MCP
σ_{ij}	Species- and energy-dependent losses due to grid and foil transmission (≤ 1)
τ_{FC}	Faraday cup aperture grid transmission (<1)
τ_{ij}	Species- and energy-dependent transmission (≤ 1)
Ω_i	Ion cyclotron frequency for species i
ω_{pi}	Ion plasma frequency

1 Introduction

Magnetic reconnection is a fundamental universal plasma process that converts energy stored in magnetic fields into particle acceleration and heating. Despite many years of study, both remotely and *in situ*, this important process is still poorly understood, in part because detection techniques have not been up to the task of measuring key reconnection phenomena. The goal of the Hot Plasma Composition Analyzer (HPCA) investigation is to support the Magnetospheric Multiscale mission (MMS) by determining the ways in which key marker species found in the solar wind and Earth's magnetosphere (H^+, He^{++}, He^+ and O^+) contribute to reconnection phenomena.

There is a large amount of literature dealing with experimental observations of reconnection as well as many papers on reconnection theory and simulations. We make no attempt to review this topic in any detail. In this volume Burch et al. (2014), Fuselier et al. (2014), and Hesse et al. (2014) give comprehensive reviews of reconnection phenomena and discuss the scientific objectives of the MMS mission. In addition to their reviews we have found papers by Shay et al. (2001), Kuznetsowa et al. (2001), Phan et al. (2003), and Drake et al. (2009) useful in formulating instrument science goals and requirements.

We begin with a short discussion of the ways in which plasma composition affects reconnection phenomena (see for example Drake et al. 2009), and why composition measurements are key to mission science objectives. We then present the specific objectives of the HPCA investigation, derive measurement and performance requirements based on these objectives, describe the design and implementation of the instrument, and present calibration data verifying HPCA performance.

By way of introduction, the HPCA is a time-of-flight (TOF) mass spectrometer designed to measure the velocity distributions of the four ion species (H^+, He^{++}, He^+ and O^+) known to be important in the reconnection process. The measurement technique is based on a combination of electrostatic energy-angle analysis with time-of-flight velocity analysis. The result is an accurate determination of the velocity distributions of the individual ion species. In order to meet the stringent scientific requirements of the MMS mission, the HPCA incorporates three new technologies. The first extends counting rate dynamic range by employing a novel radio frequency mass filter that allows minor species such as He^{++} and O^+ to be measured accurately in the presence of intense proton fluxes found in the dayside magnetopause. The second ensures that TOF processing rates are high enough to overlap with the low end of the RF dynamic range, while the third enhances ion mass resolution.

2 Science Objectives

During reconnection oppositely directed magnetic fields join and annihilate, releasing magnetic energy in the form of accelerated ions and electrons that rapidly leave the reconnection region. Reconnection takes place within a narrow ($\sim$10 km) electron diffusion region located within a much larger (hundreds to thousands of km) ion diffusion region (Fig. 1). It is the latter that is of greatest interest here primarily because ion dynamics control the rate of reconnection and the size of the reconnection region.

Ions flow into the reconnection volume at relatively low speeds proportional to the ratio of the width to length of the region times the Alfven velocity (Fig. 1). Because of the thinness of the electron diffusion region this ratio is very small and typical inflow velocities are limited to $\sim$10 km/s. As reconnection proceeds ions drift into the electron dissipation region where they are demagnetized and accelerated by reconnection electric fields into the Alfven exhaust region, creating narrow jets. Ion energies, which are proportional to the product of the Alfven velocity times their mass ($\sim m_i C_A^2$), can be very high ($\sim$100 keV) depending on plasma conditions.

Ions and electrons flowing into the ion diffusion region have large differences in gyroradii. Consequently they move very differently and tend to separate in the reconnecting volume where the magnetic field lines are tightly curved and ions become demagnetized. This leads to de-coupling of electron and ion motions particularly in the electron diffusion region where the magnetic field virtually disappears. Motions are then governed by reconnection electric fields. Because the electron scale lengths in reconnection are small, the much slower ions are relatively unimportant in the narrow electron diffusion region other than for charge conservation. Instead, the large gyroradii of the much heavier ions determine the overall size of the reconnection region that is related to the dimensional aspect ratio and the ion inertial length (Fig. 1).

The situation in reconnection is complicated not only by the large differences in gyroradii of H^+ and O^+, but also because of the variability in their relative number densities which depend on solar wind and geomagnetic activity (Geiss et al. 1978; Young et al. 1982). Yet one more reason that knowledge of ion composition is critical to understanding how ions control reconnection.

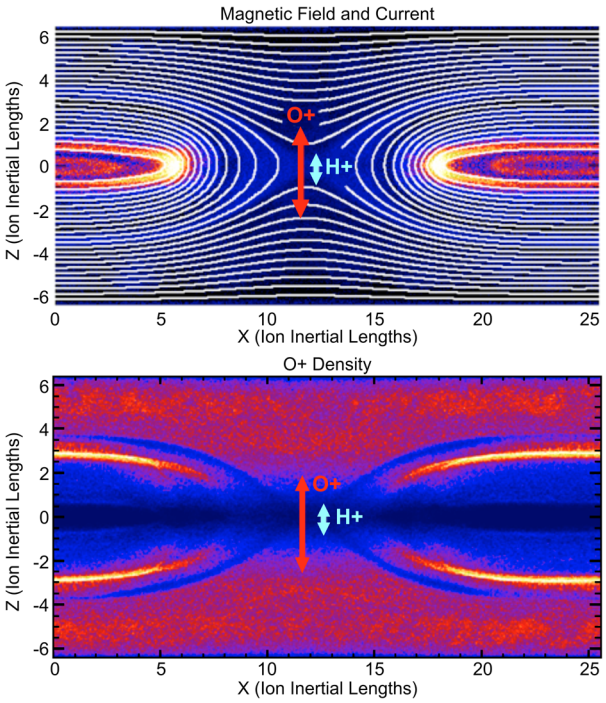

Fig. 1 *Upper panel*: Models of magnetic field lines (*white*) and current density (*red*) in the region of the x-line during reconnection. *Bottom panel*: Models of the density of O^+ (*red*) and H^+ (*blue*) during reconnection. Ordinate and abscissa are given in units of ion inertial lengths. The *vertical arrows* in both panels show the relative scale size of ion inertial length of the two species. Note the concentration of O^+ into narrow sheets in the lower panel as it is accelerated out of the reconnection exhaust region

Another species-dependent phenomenon of interest is mass transport across the magnetopause during reconnection. Obviously it is impossible to calculate the mass density of plasma being transported without knowing the identity of the ions taking part. This leads to another important HPCA science objective, namely identification of the sources of plasma undergoing reconnection. Alpha particles (He^{++}) are associated with a solar wind source, while He^+ and O^+ are terrestrial in origin, making them excellent markers. Protons may originate from either source making them useless as markers.

Here it is important to point out that the speed with which HPCA measures composition over three dimensions is one-half of a spacecraft spin period (nominally 10 s). However ion phenomena of major importance to reconnection can occur on much faster time scales ($\ll$1 s). For this reason each MMS spacecraft carries four Dual Ion Sensors (DIS), part of the Fast Plasma Investigation (FPI). The DIS are capable of measuring 3-dimensional velocity distributions of the total plasma ion content at the very high rate of 150 ms per distribution. The energy and angular ranges and resolution of the DIS and HPCA match. Since composition is not expected to change on time scales much below 10 s there is a natural division of labor between the two instruments: FPI will provide high time resolution measurements of the ion distributions while HPCA will provide complementary data on ion composition. During analysis the two data sets can be combined to give an unprecedented view of composition-resolved plasma dynamics.

Because species-dependent effects are important, it is imperative that the composition of reconnecting plasmas is measured accurately over the full range of ion velocities (Paschmann et al. 1986). This leads to the overarching science objective of the HPCA investigation, namely measuring the velocity distributions of all significant ion species (H^+, He^{++}, He^+, O^+) taking part in reconnection. In the remainder of this section we discuss quantitative considerations that go into meeting this objective.

As noted above, the overall size of a reconnection region is determined by ion decoupling and diffusion across the magnetic field. The typical scale length for the diffusion region varies with the ion inertial length $\Delta_i = c/\omega_{pi} = (\varepsilon_0 M_i/Ne^2)^{1/2}$ (in cgs units), where ω_{pi} is the ion plasma frequency, M_i is ion mass/charge of species i, N is the total ion number density and ε_0 and e are the permittivity of free space and the magnitude of the electron charge respectively. With reference to Fig. 1, the difference between O^+ and H^+ inertial lengths on the scale of reconnection is considerable (a factor of four), illustrating the need for measurements of mass-resolved velocity distributions within the ion diffusion region.

Knowledge of composition is also essential for accurate determination of the velocity distribution function $f_i(v)$ used to calculate bulk plasma parameters such as density and flow velocity (Paschmann et al. 1986; Fränz et al. 2006). This can be shown explicitly by starting with the ion energy flux $F(E)$ measured at energy E by an energy analyzer with a geometric factor G_E during an interval Δt

$$F(E) = C(E)/G_E \Delta t. \tag{1}$$

Thus energy flux is directly proportional to counting rate, making it the "easiest" parameter to measure. (In this simplified derivation vector quantities are ignored. For a more complete derivation see Collison et al. 2012.) During analysis, however, the velocity distribution of species $f_i(v)$ is usually of more interest

$$f_i(v) = C(v)/\left(G_v v^4 \Delta t\right). \tag{2}$$

The transformation from the measured counting rate into the velocity distribution is

$$f_i(v) = C_i(E) M_i^2/\left(2G_E E^2 \Delta t\right). \tag{3}$$

Using (1) this gives

$$f_i(v) = F_i(E) M_i^2/2E^2. \tag{4}$$

The point of this simple derivation is to show that a plasma sensor that measures only ion energy/charge cannot determine the velocity distribution without knowledge of ion mass/charge. This is the primary reason why a plasma mass spectrometer, such as HPCA, is essential to a mission such as MMS.

As an example of this assertion, Paschmann et al. (1986) have discussed errors in plasma measurements at the magnetopause introduced by lack of knowledge of plasma composition. In the absence of other information it is necessary to assume that all ions are protons. Paschmann et al. have shown this can lead to large errors in moment calculations which depend on ion number and mass density. An instrument without mass resolving capabilities will measure an apparent number density N'

$$N' = N_p + (M_p/M_i)^{1/2} N_i \tag{5}$$

where N_p is the proton number density and N_i the heavy ion density. As might be expected there is an error in mass density as well

$$\rho' = M_p N' = \rho_p + (M_p/M_i)^{3/2} \rho_i \tag{6}$$

where N and ρ are the true densities and N' and ρ' are densities measured by a non-mass-discriminating sensor. Paschmann et al. (1986), calculate that for plasma containing 5 % oxygen ions by number, the number density is underestimated by 3.8 % while mass density is underestimated by 45 %. Errors in velocity, temperature and pressure moments can be quite large when there is a large difference in ion drift velocities (Paschmann et al. Table 1)

Table 1 Plasma parameters requiring composition measurements for their determination

Science requirement	Equation	Measured parameters
Ion inertial length	$c/\omega_{pi} = (\varepsilon_0 M_i/N_0 e^2)^{1/2}$	Mass, density
Ion cyclotron freq.	$\Omega_i = eB/M_i$	Mass
Ion acceleration	$E_i \sim M_i c_A^2$	Mass
Alfven velocity	$c_A = B/(\mu_0 N_i M_i)^{1/2}$	Mass density
Wahlen condition	$\Delta V = f(M_i N_i, P_i)$	Mass density, ion pressure

and much smaller if the ion species have equal velocities. One important point is that the errors can be quite different for different combinations of density, velocity and temperature. Thus not only is the parameter being measured wrong, the error estimates are also wrong, sometimes by large factors. Since the fraction of O^+ can at times be as high as 20 % inside the magnetosphere (Young et al. 1982), knowledge of composition of ions drifting into reconnection at the magnetopause is essential. As a further consequence of misestimating moments, derived plasma parameters such as the ion inertial length will also be in error.

By way of a summary, Table 1 lists parameters for which ion identity and mass are essential to ensure measurement accuracy.

3 Measurement Objectives and Requirements

3.1 Measurement Objectives

HPCA objectives have been derived from science goals discussed in the previous section. Specifically HPCA must:

- Resolve plasma velocity distributions including flows and temperatures in the reconnection diffusion region within 10 s.
- Detect the decoupling of ions from the magnetic field across the reconnection region.
- Determine ion inflow and outflow velocities, plasma pressure gradients and ion anisotropies.
- Measure mass flow rates across the magnetopause during reconnection.

In most cases these measurements will be coordinated with other sensors on the four spacecraft in order to mesh particle and fields data with composition to determine global parameters such as pressure gradients and plasma beta.

3.2 Measurement Requirements

Measurement requirements are a statement of the specific parameters that must be determined in order to carry out science objectives. At the highest level these are given in the overall mission requirements: "MMS shall measure composition-resolved plasma ion distribution functions to 30 keV at least every 15 s on at least three spacecraft." This very general requirement drives much of the HPCA design. This can understood with reference to Fig. 2, which shows an idealization of characteristic ion energy distributions found in reconnection. From Fig. 2 we see that proton fluxes found in dayside reconnection near the magnetopause are extremely intense: up to $\sim 3 \times 10^9$ keV/cm sr keV, or, since this is an idealization of a

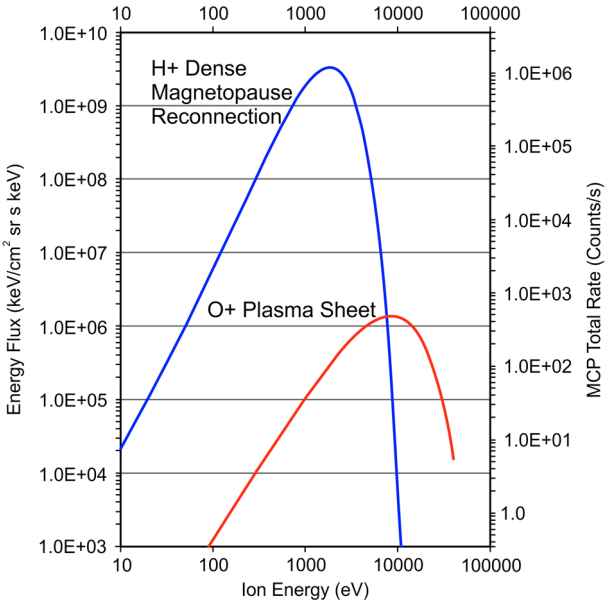

Fig. 2 Schematic representation of the peak proton energy flux in the vicinity of magnetic reconnection taking place in the dense dayside magnetopause. The O^+ distribution is characteristic of the low density magnetotail

limited amount of data, possibly higher. The distribution peaks ∼1 keV and extends to several keV. Helium ions in the magnetopause originate in the solar wind giving them energies roughly four times higher at fluxes 10 to 100 times lower.

The intense proton fluxes contrast with very diffuse O^+ and other minor ion distributions found in the magnetotail. The idealized distribution peaks at $\sim 3 \times 10^5$ keV/cm sr keV at energies ∼5 keV. Although covering the peak energy is critical, Fig. 2 makes clear that a full characterization of minor species distributions requires measurements of energy flux down to $\sim 10^4$ keV/cm sr keV at energies up to ∼30 keV.

Plasma flows in the magnetosheath, magnetopause and reconnection also put requirements on instrument angular resolution. The half-angle range of the velocity anisotropy of a flowing distribution is roughly $\Delta\theta_{1/2} \sim v_{th}/V_0 \sim 1/(\text{ion Mach number})$. The latter is expected to be ∼2 or less in the low latitude boundary layer. Then $\Delta\theta_{1/2} \sim 0.5$ radians ∼30° which requires a resolution of ∼10° to define the flow.

In summary, in order to meet science requirements the HPCA must be capable of determining the following parameters under all conditions and in all regions where reconnection occurs:

1. Ion energy from 10 eV to 30 keV with a resolution of 20 %
2. Ion arrival directions over 4π sr resolved into $\sim 20° \times 20°$ pixels
3. Ion energy flux from $\sim 10^4$ to $\sim 3 \times 10^9$ keV/cm sr keV
4. Ion velocity distributions resolved into H^+, He^{++}, He^+ and O^+
5. Complete this suite of measurements within 10 s (1/2 spacecraft spin period)

The first and second requirements set the HPCA energy and angle ranges and resolutions. The third requirement is particularly critical: it sets the sensitivity needed to detect minor species (e.g., O^+) as well as the counting rate dynamic range because of the large difference in abundance between H^+ and minor species. The fourth requirement determines mass range and resolution while the fifth sets the rate at which data is acquired and processed.

4 Performance Requirements

From the above list of measurement requirements we can derive corresponding performance requirements that will determine the detailed design of the instrument.

The four ion species of interest have mass/charge (M_i/q) ratios of $i = 1$, 2, 4 and 16 which requires relatively low mass resolution $M/\Delta M = 4$ for separation. Because the HPCA is a time-of-flight instrument we need TOF resolution $T/\Delta T = 2M/\Delta M = 8$.

The requirement that HPCA measure ion velocities in the reconnection region sets angle and energy resolution as does the goal of acquiring 3-D distributions in 10 s. HPCA energy resolution $\Delta E/E$ must be $\leq$20 % over the range $\sim$10 eV to 30 keV. Because it is easily achieved and requires only a small increase in resources, we chose to set the energy range at $\sim$1 eV to 40 keV. In order to evenly sample energy and angle, the spacecraft spin is divided into 32 equally spaced 11.25° azimuthal intervals each lasting 625 ms during which the energy range is swept. We can estimate the number of logarithmically-spaced steps per energy scan as $\mathcal{N} = (E/\Delta E)\ln(E_{\max}/E_{\min}) = 53$. Operationally it is desirable to use a binary number of steps so we chose $\mathcal{N} = 64$ which gives a spacing interval $\Delta E/E = 0.17$ at stepping rate of 9.7656 ms. Allowing for high voltage settling times gives the sampling interval live time $\tau = 8.95$ ms.

Ion flows can be resolved with an angular resolution $\Delta\alpha \sim 10°$ which happens to be the typical resolution of ESA optics. However, in order to achieve evenly distributed azimuthal samples we set $\Delta\alpha = 11.25°$.

Given the nominal MMS spacecraft spin rate of 3 rpm (20 s per revolution) a top-hat analyzer with a field-of-regard of 360° in the plane containing the spacecraft spin axis will cover 4π sr in 10 s. Ion optical considerations lead to a choice of 16 elevation samples for a resolution $\Delta\beta = 22.5°$ and a pixel size of $\Delta\alpha \times \Delta\beta = 11.25° \times 22.5°$.

The required HPCA sensitivity can be calculated using (2). The counting rate C_i for a differential directional number flux F_i and species i at energy E_j is

$$C_i(E_j) = F_i(E_j)G_{ijE}\Delta t \text{ (cts/s)} \tag{7}$$

where the "geometric" factor is slightly energy dependent, containing both an energy dependent geometric component G_j and several energy and species dependent efficiency factors:

$$G_{ijE} = G_j\tau_{ij}\varepsilon_{ij}\sigma_{ij}. \tag{8}$$

Here τ_{ij} is an energy- and mass-dependent attenuation factor controlled by the RF setting, ε_{ij} combines the efficiency of electron emission from carbon foils and MCP detection efficiency, and σ_{ij} includes transmission losses inside the TOF analyzer (TOFA) resulting from ion scattering in the foils. Details are discussed later in Sect. 6.

HPCA sensitivity is driven by the need to obtain accurate measurements of low density O^+ in the magnetotail. We know from prototype testing that HPCA is capable of a per-pixel geometric factor $G \sim$ few $\times 10^{-4}$ cm^2 sr s keV/keV. This is a reasonable rough value that would meet science requirements for the following reason. Based on Fig. 2 we choose a minimum flux $\sim 5 \times 10^4$ keV/cm^2 s sr keV to be measured over 4π sr in 1/2 of a spin period. For a precision (not accuracy) of $\sim$10 % we require a counting rate $C^{-1/2} \sim 0.1$ amounting to $\sim$100 counts per 10 s spin period or $C \sim 10$ counts/s. Using Eq. (5) and setting $\Delta t = 1s$, we estimate the required geometric factor $G \sim C/F \sim$ (10 counts/s)/(5×10^4 keV/cm^2 s sr keV) $\sim 2 \times 10^{-4}$ keV cm^2 s sr/keV.

The geometric response of a spherical or mildly toroidal tophat electrostatic analyzer (ESA) is approximately (Gosling et al. 1984; Young et al. 1988)

Table 2 HPCA performance requirements

Parameter	Variable	Required Value
Sensitivity	Energy-dependent geometric factor	3×10^{-3} cm^2 sr keV/keV (total)
	Maximum potential counting rate	20 MHz
Mass/charge	Range	1 to 16 amu/e
	Resolution ($M/\Delta M$)	4 at FWHM
Energy/charge	Range	10 eV to 40 keV
	Resolution ($\Delta E/E$)	$\leq$0.2 FWFM
	Energy range scan rate	64 log-spaced samples per 0.625 s
Angle	Field-of-regard	11.25° × 360°
	Field-of-view resolution	11.25° azimuth × 22.5° elevation FWFM
	Number of pixels over 4π sr	32 azimuth × 16 elevation
Dynamic range	Maximum detectable energy flux	$\sim 3 \times 10^9$ keV/cm^2 sr s keV of H^+
	Minimum detectable energy flux	$\sim 3 \times 10^4$ keV/cm^2 sr s keV of H^+
	Dynamic range	$\gtrsim 10^5$
Timing	3-D velocity distribution	$\frac{1}{2}$ spacecraft spin (10 s)
	2-D energy-elevation scan	625 ms
	Single sample all elevations	8.95 ms

$$G \approx A_{\text{eff}} \langle \Delta\alpha \Delta E/E \rangle \Delta\beta \ [\text{cm}^2\,\text{sr keV/keV}] \tag{9}$$

where A_{eff} is the effective aperture area including the geometric area A and the effect of transmission and efficiencies (8), $\langle \Delta\alpha \Delta E/E \rangle$ is an average response taken over the azimuthal and energy passbands, $\Delta\alpha$ and $\Delta E/E$ respectively, and $\Delta\beta$ is the elevation acceptance.

With a per-pixel geometric factor $\sim 2 \times 10^{-4}$ keV cm^2 s sr/keV, proton fluxes encountered in the dayside magnetopause can produce very high counting rates, creating problems for both the MCP (due to strip current limitations) and the TOF electronics (due to dead time effects). As we noted above, it is likely that fluxes even higher than those in Fig. 2 will be encountered during the mission. We will use $\sim 3 \times 10^9$ keV/cm^2 s sr keV as a *guideline* for the peak proton energy flux and add a reasonable margin $\sim 2\times$ to the upper limit the instrument can tolerate.

A per-pixel geometric factor of 2×10^{-4} keV cm^2 s sr/keV near the peak H^+ energy flux gives $\sim 10^6$ counts/s per sr. At any given instant however, a relatively low Mach number flow could result in total flux reaching the MCP from all directions as high as $\sim$10 times this rate or $\sim 10^7$ counts/s. Adding a factor of two margin of safety requires that the MCP and TOF electronics respond accurately to rates spread over the MCP as high as 2×10^7 s^{-1}.

Table 2 summarizes performance requirements derived in this section.

5 Instrument Overview

Because of its complexity, we introduce the HPCA in this section by taking a high level tour of the instrument. In Sect. 6 we will work through the design in detail.

The HPCA combines an electrostatic energy analyzer (ESA) with a carbon foil based TOF analyzer (TOFA) to measure ion energy/charge, angle of arrival, and mass/charge

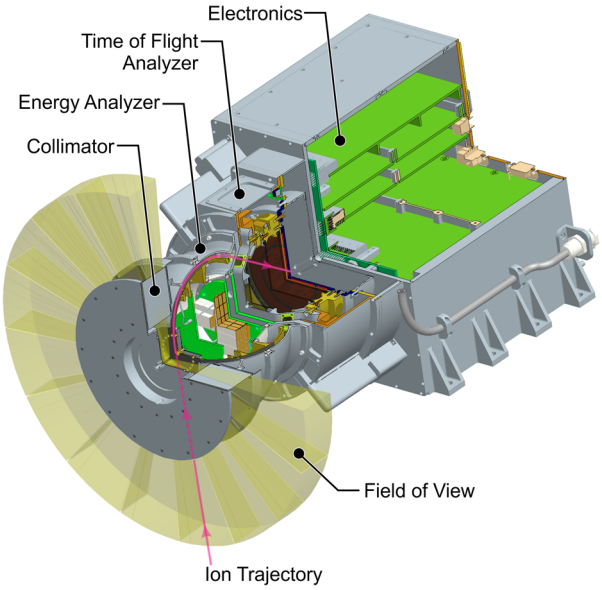

Fig. 3 Cutaway drawing of the HPCA showing its FOV and internal features. The *red line* is a typical ion trajectory passing through the collimator, electrostatic analyzer and TOF analyzer to the microchannel plate detector

(Young 1989; Gloeckler 1990; Wuest 1998). In the remainder of the paper energy/charge and mass/charge are referred to as "energy" and "mass" respectively unless otherwise noted.

Over the past 20 years our group has developed several plasma composition analyzers based on TOF (Young et al. 1989, 1990, 2004, 2007; Moore et al. 1995; McComas et al. 1998). In order to solve the sensitivity and dynamic range issues discussed in the previous section, the HPCA incorporates several innovations in both ion optics and TOF electronics that lead to significant improvements in performance compared to earlier instruments. In this section we present an overview of the HPCA as a system beginning with the sensor and working through to the electronics and instrument operation.

Figure 3 is a sectional view of the HPCA that helps to visualize key features of the sensor and electronics. Figure 4 is a vertical cross-section showing still more detail. Figure 5 is a schematic drawing of the sensor identifying the major electro-optical components and showing characteristic ion, neutral and electron trajectories.

The sensor is a rotationally symmetric 'tophat' ESA combined with a carbon-foil based TOFA. Ions enter through a grounded grid and collimator and then are guided by the tophat electric field into the ESA. High fluxes of protons entering the ESA can be selectively attenuated by a radiofrequency (RF) electric field coupled to the DC field that selects ion energy/charge.

Ions exiting the ESA are accelerated by −15 kV and then penetrate ultra-thin carbon foils (∼1 μg/cm^2) into the TOFA. Ions fly through the nearly field-free TOFA where they strike an MCP detector, resulting in an electron cloud that reaches a segmented anode. Ion charge is distributed on two anode delay lines, one of which records elevation while the other records the radial position of ions hitting the MCP. The latter information is used to correct the TOF measurement, improving mass resolution.

Delay times and ion TOF are measured by three time-to-digital converters (TDCs) that in combination give the elevation, radial position, energy and TOF for each ion. An FPGA then bins the TDC data and sends it to the Command and Data Handling (C&DH) system that compresses and packages the data before transmitting it to the Instrument Suite's Central Instrument Data Processor (CIDP).

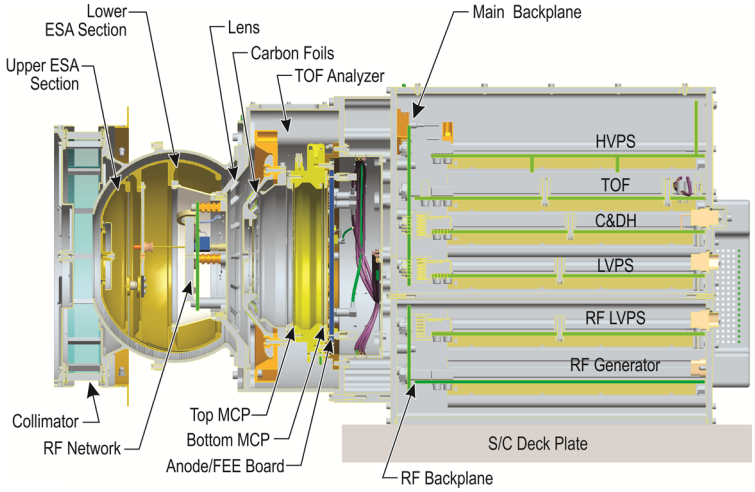

Fig. 4 Elevation cross-section of the HPCA sensor and electronics

Fig. 5 Schematic drawing of the HPCA sensor showing the main optical design elements together with characteristic ion and electron trajectories. The ion trajectories through the ESA are shown with the RF field operating to deflect protons (*black trajectories*) while transmitting O^+ (*red trajectories*)

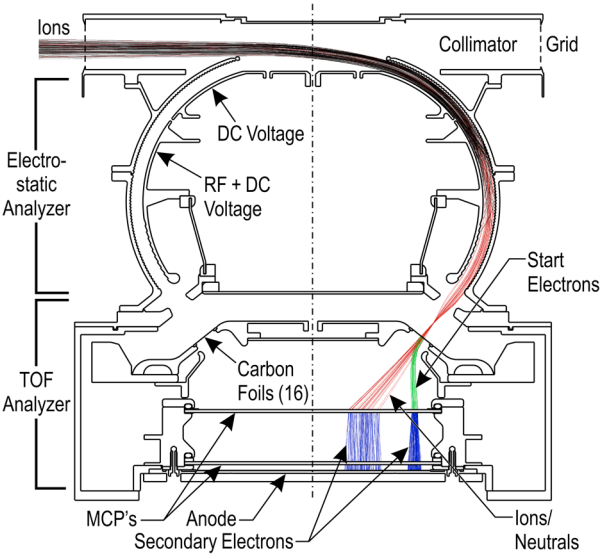

The sensor and electronics are packaged in separate compartments (Fig. 4). Mechanical, power and signal interfaces to the spacecraft all go through the electronics compartment. External features of the flight configuration are identified in Fig. 6. Figure 7 is a photograph of Flight Model 1 (FM1). HPCA is accommodated on the instrument deck of the MMS spacecraft in Bay 6 (Fig. 8) where the FOV is clear of intrusions.

This completes the general description of HPCA design features and functionality. In the following sections we discuss in detail the design and implementation of the ion optics and electronics.

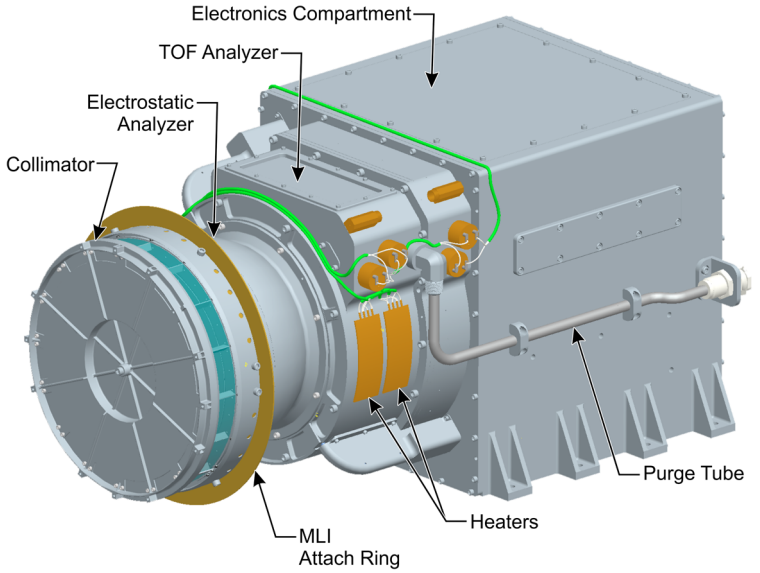

Fig. 6 Graphic rendering of the assembled HPCA flight unit showing details of the external thermal control system (MLI attach ring and heaters) as well as the purge line into the base of the MCP stack

Fig. 7 Photograph of the completed HPCA Flight Model 1

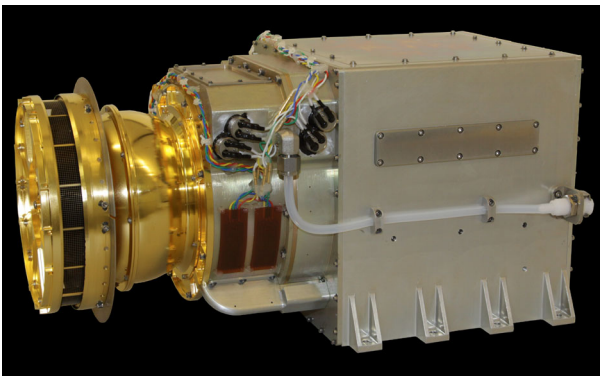

6 Detailed Design

The sensor design is described in terms of first order optics, i.e., only the principal trajectories are considered. In addition to being the simplest way to discuss the optics, our early design efforts centered on first order optics to allow many alternatives to be explored rapidly. Final design features were determined by numerical simulations.

6.1 Electrostatic Analyzer (ESA)

6.1.1 Ion Optics

We will describe the optics in the sense that particles fly through the ESA and TOFA to the detector (Fig. 5). Relative locations will be referenced as though the instrument was

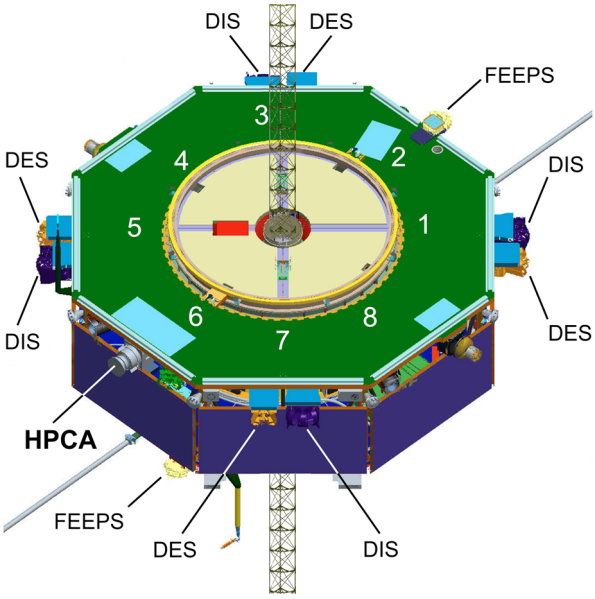

Fig. 8 MMS spacecraft showing the location of the HPCA in Bay 6 on the instrument deck

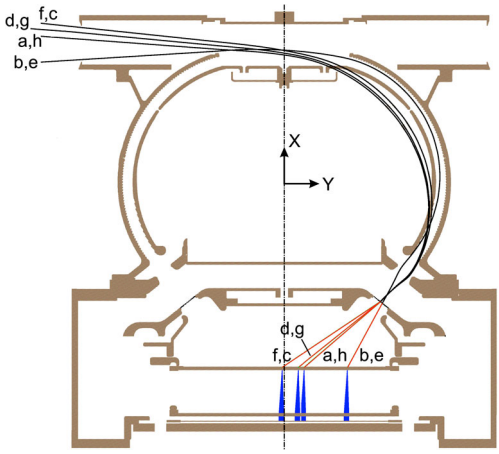

Fig. 9 Characteristic ion and electron trajectories viewed in the same plane as Fig. 5. *Black lines* are ions; *red lines* inside the TOFA correspond to both ions and neutrals. *Blue lines* leaving the top MCP are electron trajectories. *Lines* that appear to go outside of the ESA result from projection of 3-dimensional trajectories on the 2-dimensional plot

sitting vertically. Thus the collimator is "above" the ESA, which is above the TOFA, etc. We defer a description of the RF subsystem to Sect. 6.4 where the problem of dynamic range is addressed.

Figures 9, 10 and 11 show trajectories of 1 keV ions travelling through the optical system in three orthogonal planes (Fig. 9 is in the same plane as Fig. 5). Figure 9 shows pairs of ions entering the collimator over a range of azimuthal angles. They are focused by the ESA on to carbon foils located at the entrance to the TOFA. Trajectories c and f, d and g, etc. in Fig. 10 illustrate how a spread in elevation trajectories is focused in the plane orthogonal to Fig. 9. Ray tracing in Fig. 11 shows the same trajectories seen from "above," demonstrating the full 3-dimensional aspects of focusing.

Ions enter HPCA via a collimator that consists of two parallel, electrically grounded disks held together by eight posts whose cross sections are designed to prevent scattering

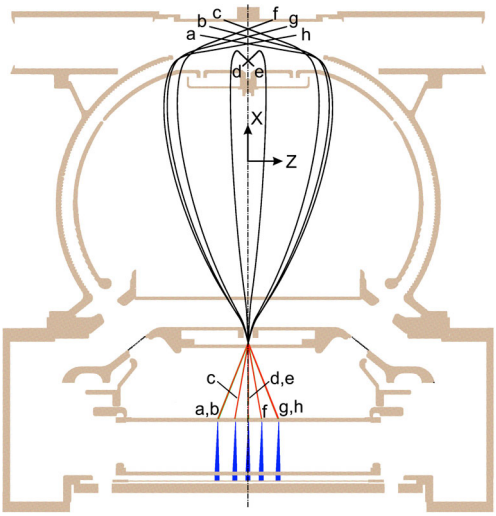

Fig. 10 Characteristic ion and electron trajectories viewed in the plane orthogonal to Fig. 9. Trajectory colors are the same

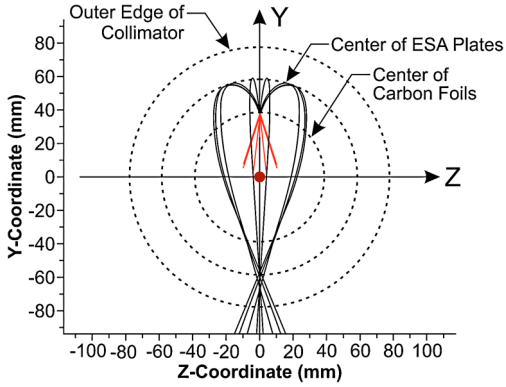

Fig. 11 Characteristic ion trajectories through the ESA and TOF regions as seen from above the collimator. *Black rays* are ions passing through the ESA while *red rays* have penetrated the foil and are inside the TOF analyzer

of incoming ions in elevation. The collimator has edges that trim the azimuthal FOV and limit trajectories entering with energies outside the ESA passband. A high transmission grid is mounted slightly inboard of the collimator to prevent RF emissions escaping that might cause electrical interference with the spacecraft.

A central disk in the collimator protrudes slightly downwards (Figs. 9 and 10) to shape the tophat electric field. Simulations were used to optimize the diameter and height of the disk in order to obtain maximum transmission while maintaining the central plane of the FOV parallel to the collimator plane and the spacecraft surface. A test of the efficacy of the collimator geometry and its relationship to the ESA and TOF optics is demonstrated in Fig. 12. Here the ions reaching the MCP detector via the collimator and ESA and within the normal energy-angle passband were flown "backwards" through the ESA to the collimator entrance. In Fig. 12 the backwards travelling beam is shown mapped back to the collimator entrance. What the figure demonstrates is that the transmitted beam, which fills the angle-energy passband, also fills the collimator. This indicates nearly ideal coupling between the collimator and ESA optics.

The ESA is comprised of two concentric mildly toroidal shells. The grounded outer shell supports the collimator assembly while the inner operates at a negative voltage proportional

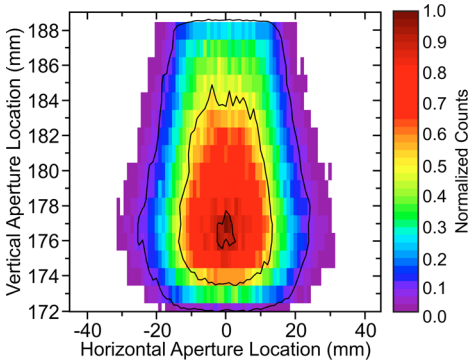

Fig. 12 Spectrogram showing a simulation of the relative number of ions able to start at the carbon foil and reach the collimator entrance via the ESA. Horizontal dimensions are centered on an elevation pixel. Vertical dimensions are height above an arbitrary reference point in the SIMION ray tracing program

to ion energy/charge. The inner shell is divided into two parts: the upper carries only the ESA DC voltage while the lower carries combined DC and RF voltages. This assembly, including the RF distribution network (Fig. 4), is suspended above the TOFA by a thin conical insulator made of the low-outgassing polymer Ultem 1000. In order to suppress any possible electromagnetic interference, the local RF distribution network resides within the inner ESA shell. High voltage is delivered to the inner shell via hollow spokes that support the inner shell assembly. Posts supporting the collimator, and spokes supporting the inner ESA, were designed to minimize blockage of the elevation pixels. That feature, together with elevation focusing (Fig. 10), resulted in the full theoretical passband of 22.5° being maintained.

Toroidal optics possess two radii of curvature (R_0 and $R_0 + R_1$ in Fig. 13) that focus ions independently in two orthogonal planes. The radii can be adjusted to obtain optimum focusing between the ESA and TOFA (Figs. 9 and 10), which yields some improvement in geometric factor over a spherical analyzer (Young et al. 1988; Gomez 2011). Since the ESA is only mildly toroidal its transmission properties can be estimated analytically to first order. This allowed us to optimize the geometric factor vs. energy-angle resolution while also matching the conditions needed for maximum transmission through the TOFA.

To first order the ESA optical design is based on (9) which is repeated here

$$G \approx A_{\text{eff}} \langle \Delta\alpha \Delta E/E \rangle \Delta\beta \ [\text{cm}^2\ \text{sr keV/keV}]. \tag{9}$$

This equation shows in a simple way the design tradeoffs between the aperture area A_{eff} and the instrument angular ($\Delta\alpha$, $\Delta\beta$) and energy ($\Delta E/E$) resolutions (smaller passbands are equivalent to higher resolution). For any given sensitivity (G), the design goal (Table 2) is to produce as large an acceptance area as possible for a given resolution.

Using results from Young et al. (1988), the purely geometric aperture area of a toroidal top-hat is approximately equal to the product of the ESA shell spacing and radius of the top-hat opening

$$A \approx \left(R_1 + R_0 \sin 15^\circ\right) \Delta R \ [\text{cm}^2] \tag{10}$$

where R_0 is the toroid's major radius, R_1 is the minor radius, ΔR is the ESA shell spacing, and 15° is the offset of the aperture from the symmetry axis. Optimization studies performed for our previous analyzers have shown that $R_0 = 4R_1$ is a good choice regardless of the rest of the ESA geometry. Then

$$A \approx R_0 \left(0.25 + \sin 15^\circ\right) \Delta R \approx 1/2 R_0 \Delta R. \tag{11}$$

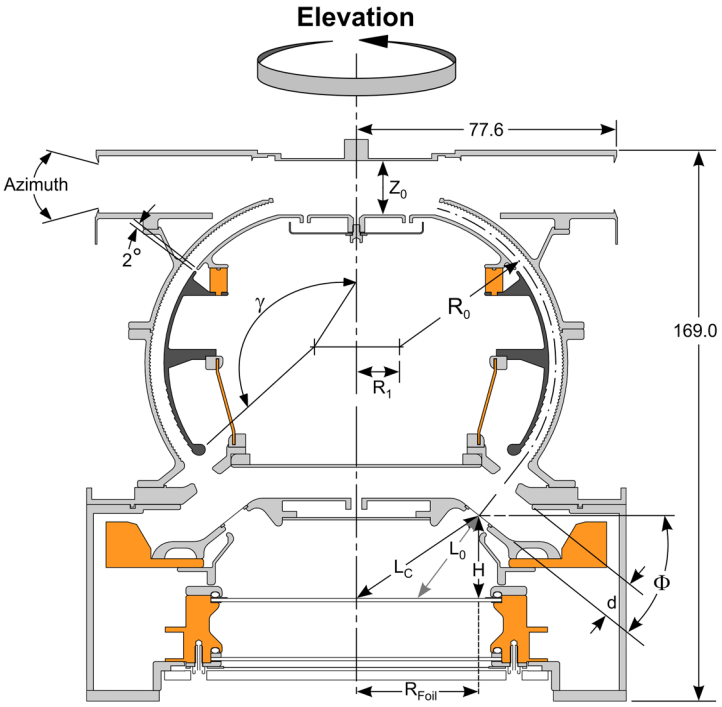

Fig. 13 Key dimensions of the sensor optics. Table 3 gives the final numerical values

For a spherical or mildly toroidal ESA, the average response over the angle-energy passband is (Gosling et al. 1984; Young et al. 1988)

$$\langle \Delta\alpha \Delta E/E \rangle \approx 1/2(\Delta R/R_0)^2 f(\gamma_{\mathrm{ESA}}) \tag{12}$$

where γ_{ESA} is the ESA bending angle (Fig. 13). The bending angle function (Gosling et al. 1984) is

$$f(\gamma_{\mathrm{ESA}}) = csc^3(\gamma_{\mathrm{ESA}}/2)\left[7/8 + \cos(\gamma_{\mathrm{ESA}}/2)\right] \tag{13}$$

which varies between 0.178 at $\gamma_{\mathrm{ESA}} = 60°$ to 0.0271 at $\gamma_{\mathrm{ESA}} = 120°$, a range that bounds all geometries of interest here. With substitutions the geometric factor can be written in terms of ESA geometric parameters

$$G \approx 1/4(R_0 \Delta R)(\Delta R/R_0)^2 f(\gamma_{\mathrm{ESA}}) \Delta\beta \ [\mathrm{cm}^2\,\mathrm{sr\,keV/keV}]. \tag{14}$$

We introduce the ESA analyzer constant

$$k = E_0/\Delta V \approx R_0/2\Delta R \tag{15}$$

where E_0 is the energy of ions entering the ESA at the center of the passband and ΔV is the voltage between the ESA shells. Increasing k increases angle and energy resolution while at the same time lowering the amount of voltage needed to transmit a given energy ion. Substituting k gives

$$G \approx 1/32\left(R_0^2/k^3\right)\Delta\beta f(\gamma_{\mathrm{ESA}}) \ [\mathrm{cm}^2\,\mathrm{sr\,keV/keV}]. \tag{16}$$

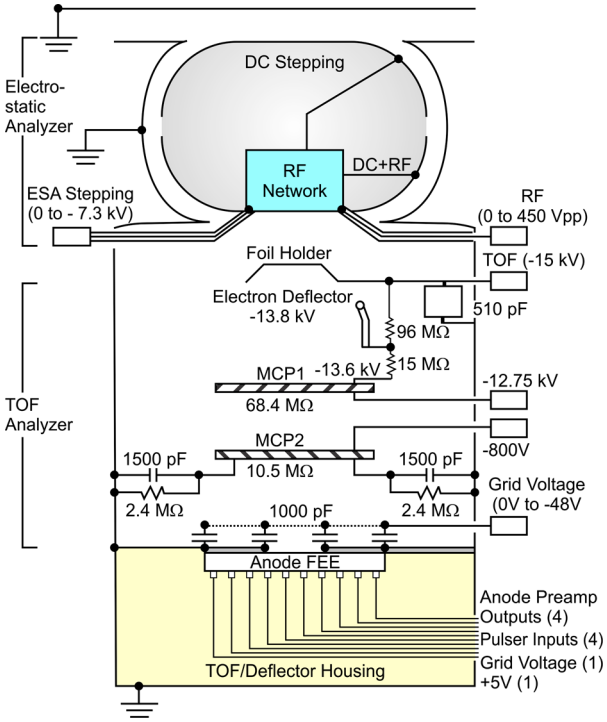

Fig. 14 Schematic diagram of high voltage distribution inside the sensor

These first order equations show the dependence of sensitivity and resolution on sensor geometry and suggest design tradeoffs. In particular, sensitivity is proportional to R_0^2, which quickly drives up instrument size for a given resolution (k = constant). For a given instrument size (fixed R_0) resolution drives sensitivity even faster: doubling resolution decreases sensitivity by nearly an order of magnitude. Increasing resolution (smaller k) has the advantage of reducing the amount of high voltage on the inner ESA shell for a given particle energy (15).

One final consideration is rejection of scattered EUV and particles outside the passbands that reach the detector causing background. Scattering can be reduced by $\sim 10^9$ using a combination of several methods. The relatively small ESA shell separation and large bending angle of 128.6° (Table 3) are such that a minimum of three bounces are required before a scattered photon or particle hits the foils. Fine serrations (Fig. 5) cut into the inner and outer surfaces of the ESA toroids, as well as copper oxide black coatings on all scattering surfaces (Balsiger et al. 1976), reduce the probability of forward scattering to the next wall by $\sim 10^{-3}$. This combination gives a total scattering reduction of roughly 10^9. The low efficiency of the MCP for EUV detection further reduces background. Similar treatment of surfaces on the CAPS and PEPE spectrometers flown on Cassini and Deep Space 1 respectively showed no evidence of background from solar EUV near 1 AU (Young et al., 2004, 2007).

6.1.2 ESA Electronics

Electronics associated with the ESA consist primarily of a DC high voltage (HV) stepping supply and a novel RF HV supply (Fig. 14). The supplies are described in detail in Sect. 7.2.3. The ESA supply generates a commandable negative voltage $-V_j$ that is applied

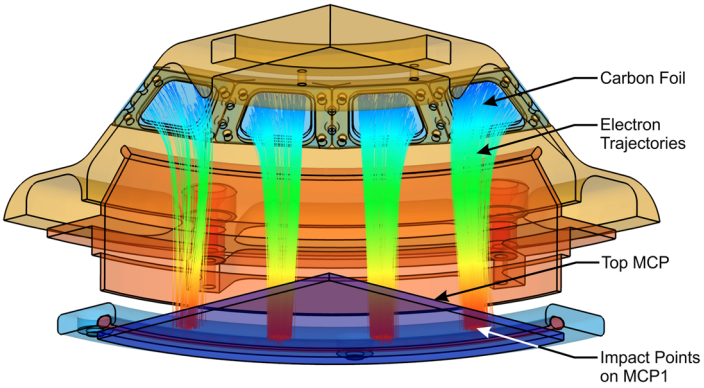

Fig. 15 Numerical simulation of the trajectories of electrons leaving the carbon foils being focused down on to the top MCP. Colors represent relative energy. *Blue* corresponds to ∼zero eV while *red* is ∼1.4 keV

to the upper and lower sections of the inner ESA toroid to select ions with energy $E_j = kV_j$. The highest applied voltage on the ESA is −7000 V across the 4.0 mm shell gap giving a maximum electric field of 1.75 kV/mm, which is well within engineering design guidelines limiting electric fields in vacuum to ≤2 kV/mm. The minimum supply voltage is −0.21 V.

6.2 Time-of-Flight Analyzer (TOFA)

6.2.1 Ion Optics

The TOFA consists of a cylindrical volume topped by 16 equally-spaced carbon foils biased at −15 kV (Fig. 5). Ions exiting the ESA are accelerated by −15 kV across a gap between the ESA and TOFA into carbon foils (∼1 μg/cm^2) mounted on 90 % transmissive 333 lines-per-inch grids. The post-acceleration of −15 kV ensures that all ion species, including those with external energies as low as a few eV, are able to penetrate the foils. Ions exit the foils either positively or negatively charged or as neutrals. (In what follows we continue to refer to the particles as "ions.") The TOFA optics are designed so that charge state doesn't appreciably affect trajectories inside the analyzer.

Ions exiting the carbon foils eject secondary electrons that are focused in three dimensions (Fig. 15) to form an image of the foil on the outer edge of the top MCP (Fig. 16). The MCP has a 79 mm active diameter and is held at −13.6 kV by a resistor divider network (Fig. 14). A tap off of the −15 kV supply was designed to maintain a nominal bias across the MCP of 900 V. It is important to get the bias voltage on the top MCP correct because once installed the divider resistor that controls the voltage (Fig. 14) cannot be changed. However during tests we found that in going from the maximum allowable instrument operating temperature of 25 C, to the lowest allowable temperature of −25 C, the resistance of the top MCP increased by as much as 35 %. This was large enough to cause arcing across the MCP. Aside from arcing, an increase of this much would also increase MCP gain to unacceptable levels as well as altering the electron deflector voltage by 270 V thereby changing the TOF internal optics. One solution to maintain the correct bias would be to restrict the temperature range (and the instrument operating range) over which the TOF voltage could operate. A better solution, implemented by the MMS project, added heaters to the HPCA to dynamically maintain the HV supply operating temperature at ∼10 C.

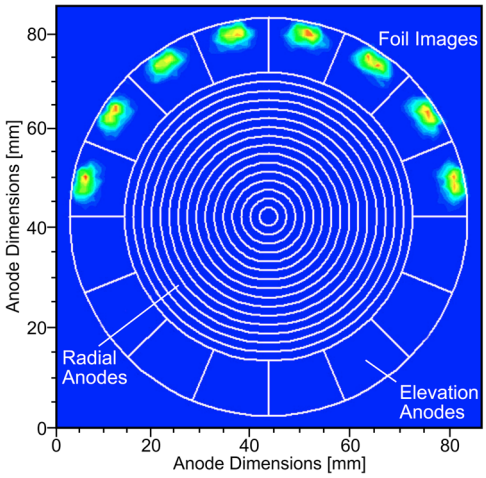

Fig. 16 Numerical simulations showing the footprint of electrons leaving the foils in Fig. 15 and striking the top MCP. Note that all of the electron images fall within the anodes outlined *in white*

The foil image on the top MCP is transmitted to the bottom MCP by focused secondary electrons (Figs. 5, 9, 16). Electron focusing in the TOFA, and from the top to the bottom MCP, is critical because the sharpness of elevation passbands depends on preventing electrons emitted by one foil from crossing over onto the adjacent image. Three-dimensional focusing is achieved by carefully shaping the back of the foil holders and by a cylindrical electrode held at −13.8 kV (Fig. 14). Figure 15 shows numerical simulations of electron trajectories leaving the foils and travelling through the flight region to the top MCP.

The bottom MCP is mounted 16.6 mm below the top MCP. The electric field between the two is designed to accelerate and tightly focus electrons on to the bottom MCP. The combined MCPs have a gain of $\sim 10^7$ at nominal operating voltages of ∼800 V across each plate. Separating the two MCPs in this way solves the problem of decoupling the signal from the top MCP at −13.6 kV to the low-voltage signal electronics associated with the bottom MCP without using large capacitors (Young et al. 2004, 2007). Prior to installation the MCPs are burned in with a UV source until ∼0.1 C of charge is extracted and the gain is stable with respect to the amount of charge extracted.

The cable carrying −15 kV from the HV supply to the TOFA is routed via a 30 kV-rated HV capacitor and HV distribution network located in a small volume inside the TOFA housing (Fig. 14). This area was particularly susceptible to HV breakdown so considerable effort was put into designing the network and surrounding region using field-tracing software as well as a large amount of testing in the flight configuration.

High voltage and signal cables pass through a sealed bulkhead separating the electronics compartment from the sensor. The bulkhead is designed to prevent sensor contamination by outgassing of the electronics. Chemical cleanliness is further ensured by a purge tube that runs along the exterior of the instrument (Fig. 6) and into the sensor at the location of the TOF analyzer. The purge rate is 0.5 to 1.0 liters/minute of high purity N_2 with the red-tag cover on and 1.0 to 2.0 liters/minute with it off. Purge continues until liftoff.

Below the bottom MCP is the combined anode and front-end signal electronics (FEE) (Fig. 4). The electron cloud from a single event leaves the bottom MCP and is collected on dual delay-line position-encoding anodes (Paschalidis et al. 2008, Byrum et al. 2010). Figure 17 is a schematic of the anodes, delay lines and TOF electronics. The photographs in Fig. 18 show details of the anodes and delay lines. Delay line electronics are discussed in more detail in Sect. 6.2.2.

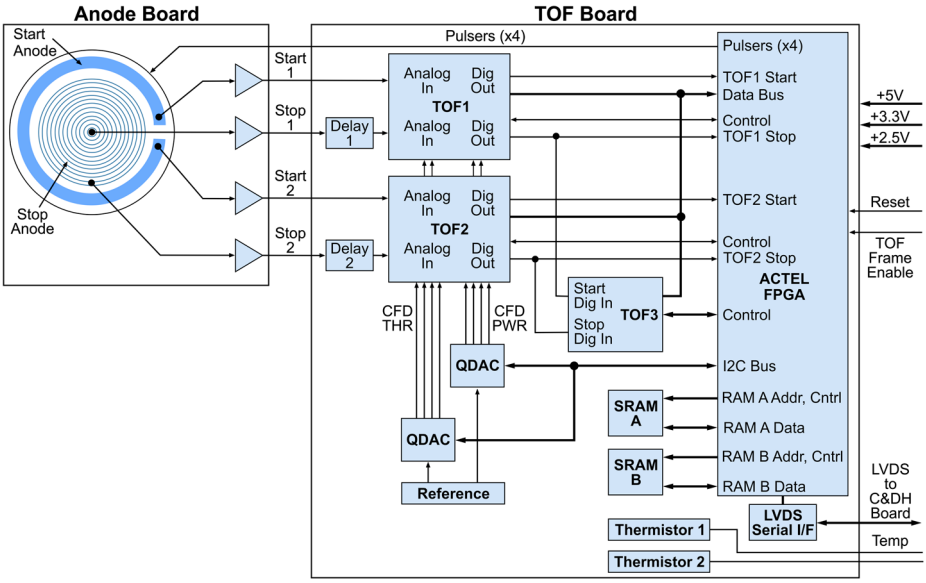

Fig. 17 Schematic diagram of the delay line anodes and TOF electronics

Charge arriving on the start anode splits into two pulses (Start_1 and Start_2) travelling in opposite directions around the start delay line. (Note that we use the convention that an underscore such as 'Start_1' indicates a signal. Those without an underscore such as 'Delay 1' indicate a circuit component.) The pulses arrive at two amplifiers separated by a time interval proportional to the position of the incident charge on the anode and thus to the ion's elevation angle. Inductive and capacitive components that couple the delay line elements code for elevation with a resolution of 32 positions although only 16 are reported in telemetry.

Similarly, the charge cloud hitting the stop anode splits into Stop_1 and Stop_2 pulses that travel along the radial delay line made up of concentric electrodes (Fig. 18) that code for 16 radial positions of which 8 are reported. Time separation of the two signals encodes the ion's radial position. In addition to position information, the average difference between Start and Stop signals gives the ion TOF from which mass is calculated. In what follows we describe in detail the position and TOF measurements.

The transit time T of an ion along a path length L in the TOFA (Fig. 19) is given by

$$T = L\left(M/2E^*\right)^{1/2}. \tag{17}$$

In engineering units (dimensions are in square brackets)

$$T\ [\text{ns}] = 22.85L\ [\text{cm}]\ \left(M\ [\text{amu}]/E^*\ [\text{keV}]\right)^{1/2} \tag{18}$$

where E^* is the total ion energy in the TOFA including a correction for energy lost in the foil (ΔE_{foil}). The total ion energy is

$$E^* = E_0 + qV_{\text{acc}} - \Delta E_{\text{foil}}\ [\text{keV}] \tag{19}$$

In considering the TOFA design it was important to bound ion flight times since they set requirements on both analyzer geometry and on high-speed TOF electronics. The fastest

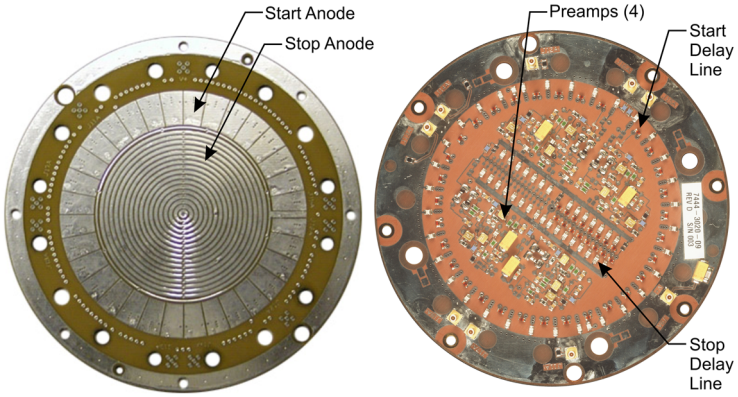

Fig. 18 Photographs of the top (*left*) and bottom (*right*) of the anode board. The top side contains the charge-collection anode pads while the bottom contains pre-amps and delay line components

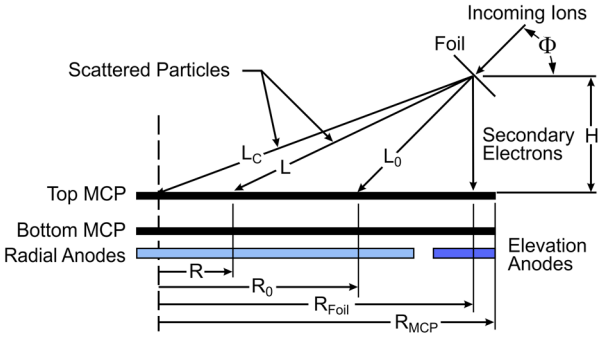

Fig. 19 Schematic of ion trajectories between the carbon foils and the MCP and anodes

ion passing through the TOFA is H^+ travelling at maximum velocity (corresponding to $E_0 = 40$ keV) along the shortest path H (for the purposes of initial estimation $H \approx 2.5$ cm). Neglecting the small amount of energy lost in the foil, the shortest H^+ flight time is 7.7 ns which leads to an acceptable lower limit of 5.0 ns.

The slowest ion through the flight region is O^+ at $E_0 \sim 1$ eV incident on the ESA. Here another operational constraint comes into play. In case there are problems operating at the highest acceleration voltage of -15 kV we want the TOF to be able to function at voltages as low as $V_{acc} = -12$ kV. At that voltage we would have degraded but acceptable mass resolution. At -12 kV O^+ would lose about 5 keV in the foil (Allegrini et al. 2006) so that $E^* \approx 7$ keV. Then $T_{max} \approx 138$ ns giving $L_{max} \approx 4.0$ cm. It is relatively easy for the TOFA electronics to measure longer times-of-flight so the upper bound was set at 256 ns. This leads to a maximum allowable upper limit on path length across the TOFA of 7.4 cm. In summary, ion times-of-flight between 5 and 256 ns provide acceptable timing limits for the electronics and dimensions for the optical geometry (viz., 2.5 to 7.4 cm from foils to MCP).

One important point about plasma mass spectrometers flown in the Earth's magnetosphere is that attaining high mass resolution *per se* is not important. Since the target ion species are well known (H^+, He^{++}, He^+, and O^+) only enough resolution is needed to identify these ions. This simplifies the mass spectrometer design and reduces resources significantly compared to a high resolution device designed solely for mass spectrometry.

Mass resolution is limited by TOF peak broadening arising primarily from the width of the ESA's energy and angle passbands. An additional source of broadening is energy and angle scattering in the carbon foils. The spread in angle translates into a spread in the ion path length $\Delta L/L$ while the energy spread $\Delta E/E$ disperses times-of flight directly. Ignoring the relatively small electronic timing errors, the TOF spread is

$$\Delta T/T \sim \left[(\Delta L/L)^2 + (\Delta E/E)^2\right]^{1/2}. \tag{20}$$

There is no practical means of reducing the contribution of energy spread to peak broadening. However it is possible to correct for some of the path length differences if the ion position on the MCP is known. Knowing the radial position allows a corrected path length to be calculated. However for this to work the position of each ion must be determined individually and "on the fly" as each event occurs—statistical measurements, which are much easier to make, will not suffice.

6.2.2 TOF Measurement and Position Encoding

With reference to Fig. 17 (Paschalidis et al. 2010), electrons leaving the foils following ion impact produce two signals (Start_1 and Start_2). Some nanoseconds later ions strike the MCP producing Stop_1 and Stop_2 signals. These are delayed 23 ns and 36 ns (Delay 1 and Delay 2 in Fig. 17) respectively in order to ensure that no timing ambiguities arise between starts and stops. Start and stop signals pass through constant fraction discriminators (CFD) to the three ASICS (CFD thresholds can be adjusted in flight). The TOF1 and TOF2 ASICS (Paschalidis et al. 2002) then measure the delays between opposite ends of the start and stop delay lines and pass this information to the FPGA (Fig. 17).

Ion TOF and position calculations then proceed as follows. The uncorrected TOF is measured by the TOF1 and TOF2 ASICs using the delay T_1 between the time a start pulse reaches the Start_1 end of the anode, and the time the corresponding stop pulse reaches the center of the stop anode (Stop_1) plus Delay_1 (Fig. 17). Similarly T_2 corresponds to the delay between the time the start pulse reaches the Start_2 end of the anode, and the time the stop pulse reaches the outer ring of the stop anode (Stop_2) plus Delay_2.

The raw, uncorrected ion time-of-flight T_U is then

$$T_U = \frac{1}{2}(T_1 + T_2) - \frac{1}{2}\Delta T_{\text{Start}} - \Delta T_{\text{Stop}}\ [\text{ns}] \tag{21}$$

where ΔT_{Start} and ΔT_{Stop} are the times taken for signals to cross the entire start and stop delay lines respectively, and ΔT_1 and ΔT_2 are Delay_1 and Delay_2 times respectively (Fig. 17). Although T_U is measured from delays on the start and stop anodes, it is purely a TOF measurement that does not depend directly on either the β or R positions. (Note that in all of these equations the factor $\frac{1}{2}$ appears because the quantity is an average of the two indicated times.)

The time corresponding to the radial position R of an ion striking the MCP is calculated using only the TOF3 ASIC and the difference in signal arrivals on the stop delay line

$$R = \frac{1}{2}(\Delta T_{\text{Stop}} - \Delta T_1 + \Delta T_2) - \frac{1}{2}T_3\ [\text{ns}]. \tag{22}$$

(Actual radial and elevation positions are determined from time-based look-up tables rather than a calculation.) Using data from all three TOF chips we obtain the time corresponding to the elevation angle

$$\beta = \frac{1}{2}(T_2 - T_1) + R + \frac{1}{2}(\Delta T_{\text{Start}} - \Delta T_{\text{Stop}} + \Delta T_1 - \Delta T_2)\ [\text{ns}]. \tag{23}$$

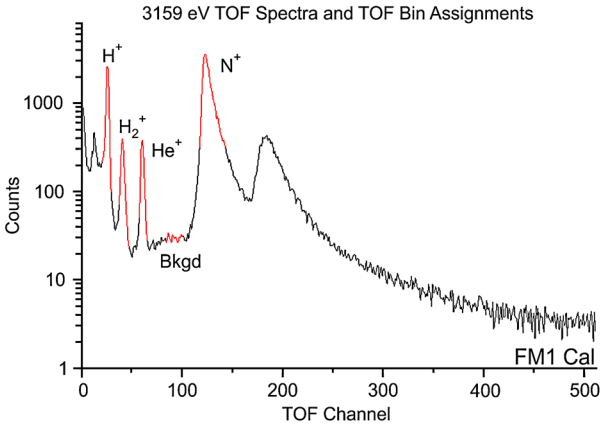

Fig. 20 TOF spectrum for four ion species and background (H_2^+ is a substitute for He^{++} and N^+ is a substitute for O^+). *Red areas* demarcate bins that define ion species and background. The *peak* at ~200 ns corresponds to N_2^+

The final value of β is calculated in the TOF FPGA

$$\beta = \frac{1}{2}(T_2 - T_1 - T_3) + \Delta T_{\text{Start}} \text{ [ns]}. \tag{24}$$

The value of R at which an ion strikes the MCP can be used to correct the apparent ion path length L to what it would have been (L_0) had the ion remained on the nominal central trajectory (see Fig. 19 for geometry). The distance from foil to MCP at the measured radial distance is

$$L = \left[H^2 + (R_{\text{Foil}} - R)^2\right]^{1/2} \text{ [mm]}. \tag{25}$$

The radius from the MCP center to the foil center is $R_{\text{Foil}} = 36.7$ mm, while the height of the foil center above the MCP is $H = 24.6$ mm. Substituting in (25) gives the path length in mm for any value of R

$$L = \left[24.6^2 + (36.7 - R)^2\right] \text{ [mm]}. \tag{26}$$

Using the measured path length we can obtain the corrected TOF value T_0

$$T_0 = T_{\text{U}}(L_0/L) \text{ [ns]}. \tag{27}$$

The value T_0 is used to address one of 512 bins which is incremented for each event. The bins are bracketed into five energy-dependent channels, one for each species plus background. Figure 20 is a sample TOF calibration spectrum showing TOF brackets. The flight software allows the TOF correction feature to be turned off for calibration purposes. The bin locations can be moved to detect other species such as O^{++}.

The correction process described above improves TOF peak resolution by 60 % at 1 keV. Figure 21 shows TOF peaks from stop rings 1 (the innermost) and 7 (the outermost) separated by 47 ns edge-to-edge at FWHM. If the counts from each ring (1 through 7) were added together without corrections the peak profile would be smeared out. The corrected peak is only 12 ns wide at FWHM demonstrating the efficacy of the correction process.

At this point in the data flow ions have been binned according to TOF (512 channels) and elevation (16 angles). Additional counters record the number of raw start and stop events and the number of valid coincident events processed by the FPGA. Start and stop counters have dead times of <250 ns, which allows them to be used to correct for the slower 2 μs dead time associated with coincident TOF signal processing. Processed events are then transmitted to the C&DH system once each spectrum (625 ms). The next steps in data processing take place in the C&DH system discussed in Sect. 8.2.

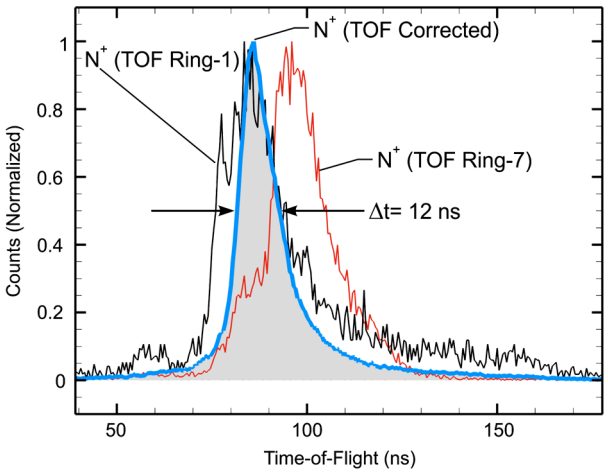

Fig. 21 Normalized TOF spectra from the prototype HPCA. Data were taken using eight discrete annular rings to detect stop events rather than the delay line technique incorporated in the Flight Models

6.3 Optimization of the Combined ESA/TOFA Optics

With reference to Figs. 5 and 13, to first order there are six geometric constraints on the match between the ESA and TOFA geometries:

- ESA radius, gap between toroidal shells, and bending angle
- High voltage gap between the ESA exit and TOFA entrance
- Ion path length from the foils to the MCP
- Radius of commercially available MCPs

The last constraint is particularly important because dimensions of standard commercial MCPs are set by the manufacturer and are not available in a wide range of values without considerable expense.

The central ion trajectory leaving the ESA exit will reach the center of the carbon foils if

$$R_{\text{exit}} = R_{\text{foil}} + L_{\text{gap}} \sin\left(\gamma_{\text{ESA}} - 75^{\circ}\right) \text{ [mm]} \tag{28}$$

where R_{exit} is the radius of the center of the ESA exit, R_{foil} is the radius to the center of the foils, and L_{gap} is the spacing between the ESA exit and the center of the foil surface. (Extension of calculations to include the entire width of the foil is carried out using numerical simulations.) R_{exit} is related to ESA geometry by

$$R_{\text{exit}} = R_1 + R_0 \cos\left(\gamma_{\text{ESA}} - 75^{\circ}\right) \text{ [mm]}. \tag{29}$$

In the 2-dimensional view in Figs. 5 and 13, a lens placed 8 mm behind the ESA exit focuses ions on to the foils (Fig. 9). (Although not apparent in the figure, because of the sensor's cylindrical symmetry there are in fact 16 lenses equally spaced around the grounded exit.) The exit lens is designed to give optimum focusing at about 1 keV, which is the point where ion trajectories become less influenced by the accelerating TOF electric field. Exit lens location is also constrained by the engineering rule-of-thumb that the electric field across a vacuum gap should be <2.0 kV/cm.

The foil radius must match approximately the outer radius of the MCP sensitive area (Fig. 19) so that electrons leaving the foil register the pixel location of ions entering the

Table 3 Key HPCA optical dimensions

Parameter	Symbol	Dimension
Outer collimator radius	–	77.58 mm
ESA poloidal radius	R_0	47.56 mm
ESA poloidal minor radius	R_1	11.89 mm
ESA toroidal radius	$R_0 + R_1$	59.45 mm
ESA toroidal/poloidal ratio	R_0/R_1	4.0
ESA shell gap	ΔR	4.00 mm
Top-hat spacing	Z_0	16.20 mm
ESA bending angle	γ_{ESA}	128°
Angle between ESA exit and foil normal	Φ	51.44°
Distance grounded lens to TOFA foil	d	12.08 mm
Central foil radius	R_{Foil}	36.66 mm
Height of TOFA flight region	H	24.62 mm
Distance from foil normal to MCP	L_0	31.4 mm
Distance from foil to MCP center	L_C	44.16 mm
Sensor height	—	169 mm

ESA (Fig. 16). This gives

$$R_{\mathrm{foil}} \approx R_{\mathrm{MCP}}\ [\mathrm{mm}]. \tag{30}$$

Based on these considerations R_{MCP} was chosen to match the standard Hammamatsu Model F1942-04 sensitive radius of 39.5 mm (outer mechanical radius = 43.35 mm).

Taken together, Eqs. (28), (29) and (30) define the optimized TOFA optical dimensions. The distance from the foil center to the top MCP is related to the longest flight path through the TOFA, namely the one from foil center to MCP center

$$H = \left(L_C^2 - R_{\mathrm{MCP}}^2\right)^{1/2}. \tag{31}$$

The central trajectory is the normal from the foil surface to the MCP

$$H = L_{\mathrm{normal}} \sin\left(\gamma_{\mathrm{ESA}} - 90^\circ\right). \tag{32}$$

There are three unknowns and two independent equations that determine the dimensions of the TOFA. Detailed numerical simulations taking into account ion scattering were used to confirm the first order design. The design was then tweaked for maximum transmission over the full range of energies and species for a given set of dimensions. With reference to Figs. 13 and 19, Table 3 contains the final dimensions for the combined ESA and TOFA.

6.4 Dynamic Range

6.4.1 Introduction

As discussed earlier, intense proton fluxes can potentially produce counting rates as high as 20 MHz at the nominal peak of the energy distribution (Fig. 2). This creates two problems related to dynamic range. The first is potential current saturation of the MCP resulting in reduced gain and lost signal. The second is the potential inability of the TOF processing electronics to keep up with high rates corresponding to coincident rate dead times ~100 ns.

At such high rates uncorrelated ("accidental") start and stop events can tie up the processing capability of TOF electronics, resulting in high rates of cross-talk between adjacent TOF channels. In particular the high proton signal will completely drown out minor species such as He^{++} and O^{+}.

One solution might be to place two different sized apertures at locations around the entrance: Large apertures for low fluxes and small apertures (e.g. $\sim$1 % of the large) for intense fluxes. However the large apertures would still transmit the same flux per unit area to the detector, causing local saturation, while the smaller apertures would reduce the sensitivity of half (or more) of the instrument, making minor species detection more difficult.

The ideal solution is to reduce proton fluxes to manageable levels while maintaining minor species fluxes close to ambient levels. This approach requires placing what is, in effect, a low-resolution mass spectrometer in front of the primary TOF mass spectrometer in order to separate protons from minor species (He^{++}, He^{+} and O^{+}). Such an arrangement could attenuate intense proton fluxes while transmitting heavier species. Burch et al. (2005) have developed what is essentially a low-resolution mass filter using a radiofrequency (RF) technique similar to the principle behind quadrupole mass spectrometers.

To get some idea of the requirements for the RF system, assume that the maximum total proton flux reaching the MCP is 2×10^7 ions/s. If each ion produces on average 2 electrons from a foil then the number of particles striking the MCP is $\sim 6 \times 10^7$ s^{-1} (including the incoming ion). In order to have optimal signal amplitudes for the TOF electronics the HPCA MCP is operated at a gain of $\sim 10^7$. At this rate and gain the signal current exiting the bottom MCP is $\sim$(6×10^7 particles/s $\times 10^7$ electrons/particle) $\times 1.6 \times 10^{-19}$ C/particle $\sim 10^{-4} C/s = 100$ μA. In order to have a linear output, the MCP signal current should be limited to $<$10 % of strip current (MCP bias voltage divided by resistance). This amounts to an MCP resistance of $\sim$10 MΩ for the bottom MCP which is what led us to choose the Hammamatsu Type 1942-04 MCP whose resistance can be specified. For HPCA we chose $\sim$70 MΩ for the top MCP and 12 MΩ for the bottom.

A second issue is current density on the MCP. The tight focusing of electrons (about 0.25 cm^2 per pixel in Fig. 16) can lead to current densities $\sim$100 μA/cm^2 which the selected MCP is able to support over a few pixels. A third problem area is the TOF electronics processing rate. We are using the best available custom ASICs, designed and built by APL (Paschalidis et al. 2002). The dead time for processing valid TOF and position location events is $\sim$2 μs which puts a practical limit of $\sim$0.5 MHz for accurate measurement.

In summary, based on considerations of MCP current saturation and TOF processing speed the RF system needs to reduce proton fluxes by at least a factor of ten.

6.4.2 Attenuation Using Radio Frequency Selection

Our approach to limiting proton fluxes is to turn the ESA into what is effectively a low-resolution RF ion mass spectrometer (Burch et al. 2005) operating independently of the TOF mass spectrometer. The RF principle can be understood with reference to Fig. 22, which shows an idealized case of a sinusoidal RF electric field applied to parallel conducting electrodes placed at ± 1.0 and parallel to the x-axis in the figure. In this simple example the RF amplitude and frequency are tuned so that on average the faster protons see only a single RF cycle, causing them to be deflected by a large amount. The heavier, slower O^{+} ions see many oscillations of the electric field which tend to cancel each other out resulting in small deflections and high transmission.

In the HPCA, as in all ESAs, a DC voltage corresponding to the desired energy is applied to the inner dome (see Eq. (15)). A sinusoidal RF voltage of selectable amplitude and

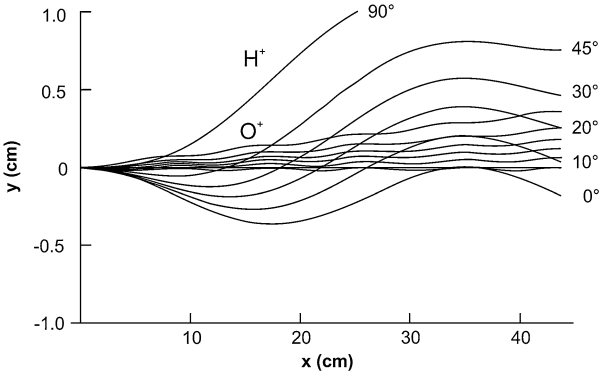

Fig. 22 H^+ and O^+ trajectories responding to an RF electric field between two conducting parallel plates located at $y = \pm 1.0$ and parallel to the x-axis. Trajectories are identified by the phase angles at which ions enter the RF field

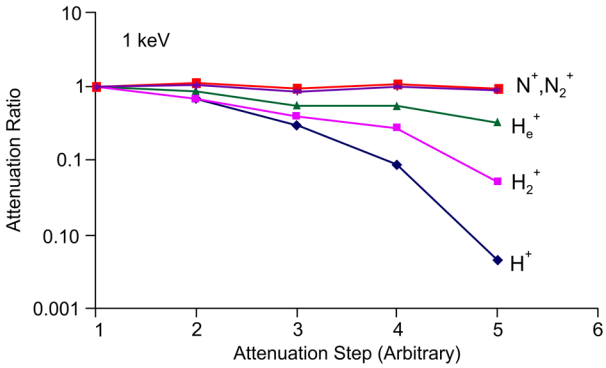

Fig. 23 Attenuation response of five ion species incident on the prototype ESA at 1.0 keV. Attenuation steps are arbitrary combinations of frequency and amplitude chosen to demonstrate attenuation for a range of mass/charge from 1 to 28

frequency is added to the DC voltage and applied to the lower part of the ESA (Fig. 5). Protons entering with a given energy move through the ESA in a length of time corresponding to about one-half an RF oscillation period. The protons experience a slowly varying field that deflects them to the side of the ESA. The number deflected, and hence the amount of attenuation, depends on the choice of RF amplitude and frequency.

Heavier ions such as O^+ with the same energy as protons travel more slowly through the ESA, encountering multiple oscillations of the electric field which modify the trajectory slightly but tend to cancel out (Fig. 22), allowing ions to travel through the ESA with minimum deflection. In the ray-trace simulation shown in Fig. 5, H^+ and O^+ ions enter the ESA with the same energy. Protons (black trajectories) immediately hit the lower part of the ESA to which RF + DC voltage is applied. Oxygen ions (red trajectories) are transmitted without appreciable losses. Intermediate mass ions (He^{++} and He^+) are partially attenuated.

The highest proton fluxes found in the magnetosheath extend from approximately 0.5 to 4 keV (Fig. 2). Therefore RF attenuation is designed to operate over this range. Although the choice of frequencies is limited to 16 fixed steps, the amplitude can be set precisely by a 12-bit digital-to-analog converter (DAC). While the ESA uses 63 steps to cover the energy range 1 eV to 40 keV, the RF is applied to only 14 of those steps covering 0.5 keV to 4.0 keV.

Figure 23 shows beam data for several ion species at an energy of 0.995 keV corresponding to the nominal peak where attenuation is most critical. We emphasize that the fraction of flux attenuated has been shown by numerous tests and calibration to be highly repeatable. The RF frequency and amplitude combinations are given in Table 4. (Note that tests of the HPCA *prototype* used to collect data for Fig. 21 were made at a laboratory beam energy of

Table 4 RF peak-to-peak voltage and frequency

ESA Step No.	DC Voltage (V)	Ion Energy (eV)	RF Frequency (MHz)	RF Amplitude (Vpp)
36	−94.7	515.9	5.1	127
37	−111.7	608.5	5.1	127
38	−131.7	717.8	5.1	127
39	−155.4	846.7	5.1	127
40	−183.3	998.8	5.2	131
41	−216.2	1178.2	5.4	135
42	−255.0	1389.8	5.5	152
43	−300.8	1639.3	5.8	177
44	−354.8	1933.7	5.9	245
45	−418.5	2281.0	6.1	294
46	−493.7	2690.6	6.1	377
47	−582.3	3173.8	6.1	377
48	−686.9	3743.7	6.1	377
49	−810.3	4416.0	6.1	377

1.0 keV. Test and calibration of the Flight Models were carried out at fixed pre-programmed energy levels. The level nearest 1.0 keV is 0.995 keV hence the difference in ion energies between Figs. 21 and 23.)

Figure 23 demonstrates proton attenuation by factors up to ∼330. The data also indicate that at these settings solar wind He^{++}, for which H_2^+ is a stand-in, is attenuated by a factor of 10 or less at ∼1 keV. The peak of the He^{++} distribution is roughly four times higher where attenuation will be considerably reduced. In any case the loss in counting rate of He^{++} is compensated by an improvement in signal-to-noise ratio (SNR). Finally, as expected from theory and ray-tracing, heavy ions such as N^+ (a stand-in for O^+) and N_2^+ are transmitted without any attenuation.

One important feature of the attenuation process calling for careful calibration is apparent in Fig. 24. The attenuated passbands (Figs. 24b and 24d) are shifted relative to the nominal passbands (Figs. 24a and 24c) but maintain their shape, i.e., resolution remains the same. Calibration data such as this allows the correct energy and flux of the attenuated ions to be recovered during analysis. The shift in the attenuated distributions can be attributed to ion trajectories just entering the ESA that are deflected by the RF field through angles and energies not ordinarily transmitted through the ESA in the DC mode (e.g., rays resembling f and c in Fig. 9).

6.4.3 High Counting Rate Capability

The RF system will be operated continuously in Fast Survey mode over the pre-selected parts of the orbit where reconnection is judged likely to occur (see Sect. 8.1.2 for a full discussion of HPCA modes). On other parts of the orbit HPCA will be operated in Slow Survey mode. In this operational scenario there are three ways in which proton fluxes might exceed the planned maximum rates. The first is where the flux maximum is above model rates in Fig. 2. The second is when reconnection occurs outside the pre-planned regions—during a strong magnetic storm, for example, when the magnetosphere collapses and the instrument is not in an RF mode. The third is when large fluxes are encountered in Slow

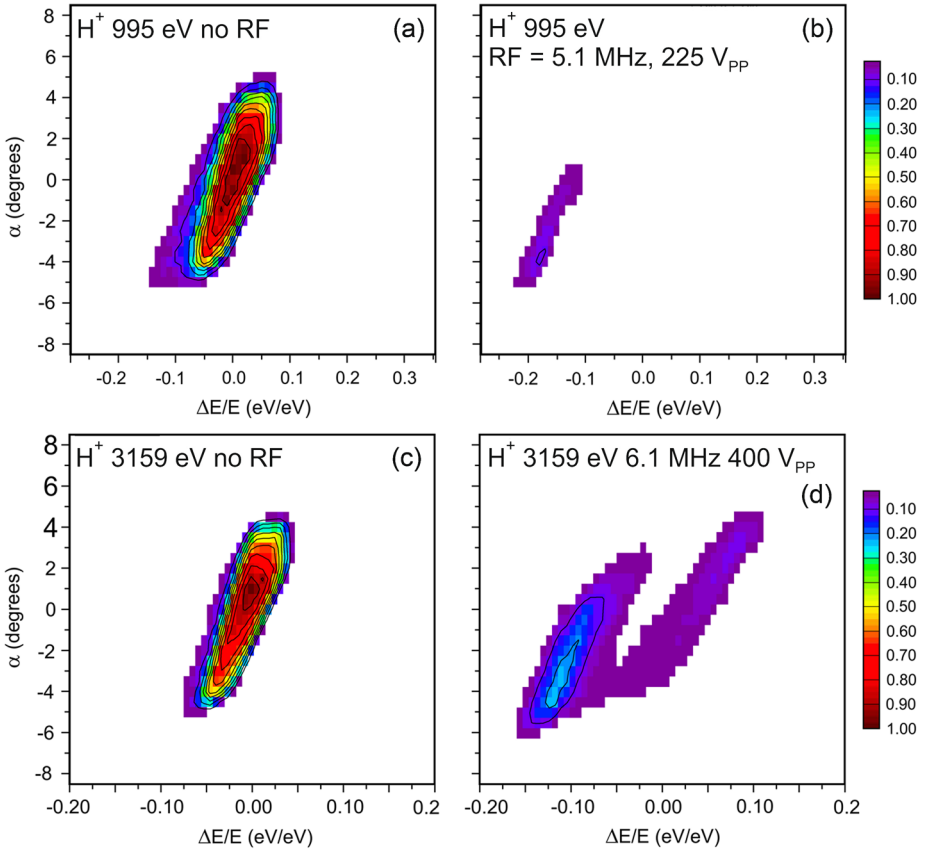

Fig. 24 Azimuth-energy passband at 0.995 keV without (**a**) and with (**b**) RF applied. Passbands at 3.159 keV without (**c**) and with (**d**) RF. The RF settings at 0.995 keV are 5.1 MHz and 225 Vpp. For 3.159 keV they are 6.1 MHz and 400 Vpp. The normalized scale for transmitted flux is on the right

Survey mode. Although RF is by far the best way to increase dynamic range in planned scenarios, it is also important to have some back-up capability to detect and process events at as high rates as possible.

The design goals for the start and stop counters were 200 ns and 3.0 μs dead times respectively for correlated events in the TOF1, TOF2, and TOF3 ASICs. Figure 25 shows linear fits to FM1 calibration data for rate in vs. rate out at relatively low rates while Fig. 26 shows data taken over a wider range of rates. Dead times are the same in both plots: 100 ns for Start_1 and Start_2, 1 μs for TOF1, and 2 μs for TOF3. At low rates the TOF electronics are non-paralyzable, i.e., if a second event arrives while the first is being processed the second event is ignored. The measured count rate C_M as a function of the true rate C_T (measured by the Faraday cup), for a dead time τ is

$$C_M = C_T/(1 - \tau C_T). \tag{33}$$

Equation (33) was used to fit the linear portion of data plotted in Fig. 25 where dead time effects are not important. Figure 26 shows the entire data set including non-linear portions where dead time effects are important. Data were not taken at beam currents above 1.3 pA at which point the instrument would be completely saturated.

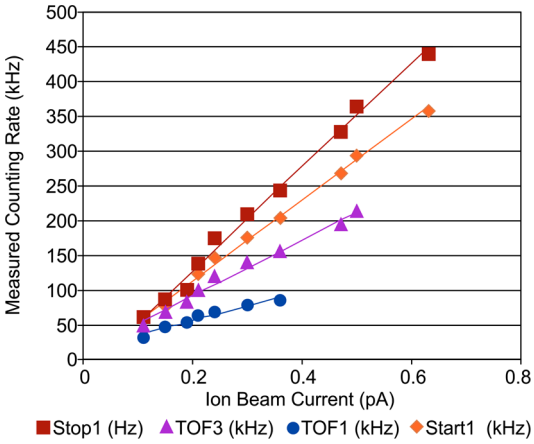

Fig. 25 Start_1, Stop_1, TOF1 and TOF3 counting rates plotted over a linear range vs. Faraday cup current in pA

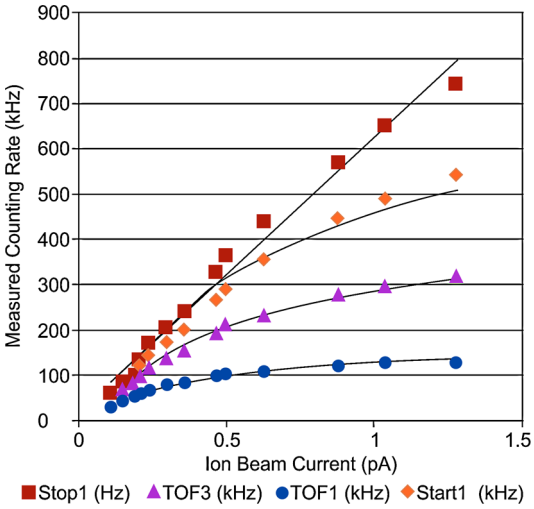

Fig. 26 Full range of Start_1, Stop_1, TOF1 and TOF3 counting rates plotted with the same dead times as in Fig. 25

7 Electronics

7.1 Electronics Housing

The electronics housing (Figs. 3 and 4) holds six printed circuit boards (PCBs) arranged parallel to the spacecraft deck to provide the best thermal pathway for dissipating heat to the spacecraft and surroundings. Conventional circuits such as HV, low voltage, and digital processing communicate through connections to the main backplane. In order to isolate RF pickup in the digital and low-level signal circuits, the RF LVPS and RF generator boards are located in a separate shielded compartment with its own shielded backplane.

The structure of the electronics housing carries the mechanical load of the cantilevered sensor and provides all mechanical and thermal interfaces to the spacecraft deck (Fig. 4). This design simplifies mounting but requires a very rigid structure to support the sensor compartment. To that end, the housing is machined out of a single block of aluminum with removable walls on top (for HV access) and at the rear (for PCB mounting and removal).

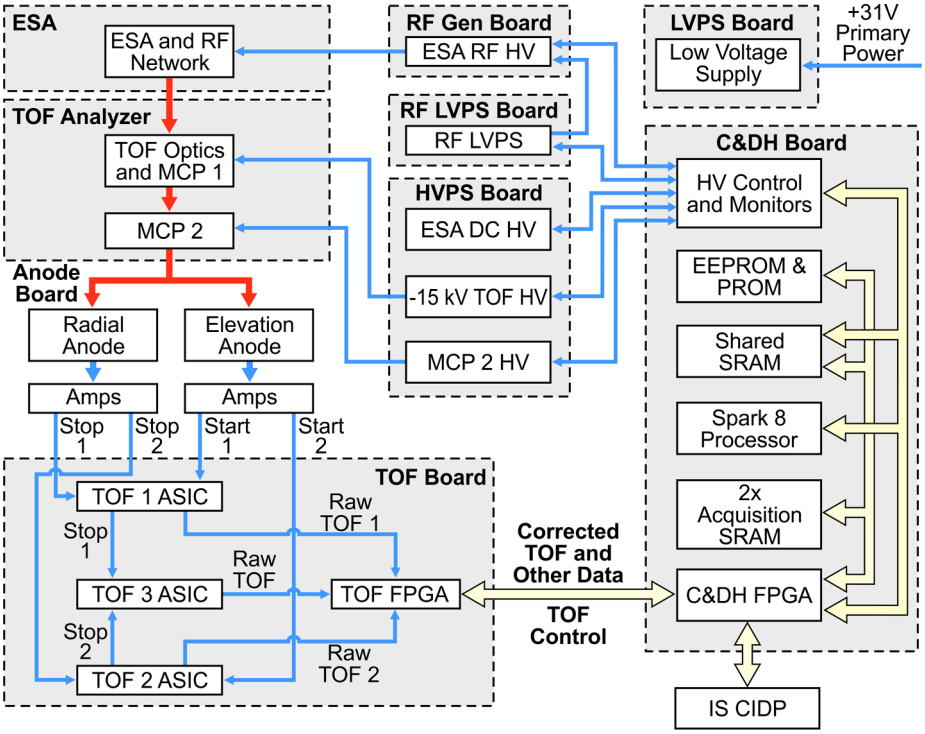

Fig. 27 Block diagram of the electrical system. *Gray areas* represent individual printed circuit boards or optical subsystems

During vacuum testing there is relatively little time for the unit to outgas completely so a high-throughput ventilated cover is substituted for the normal solid top wall.

Typical wall thickness of the aluminum housing is 3.8 mm primarily for radiation shielding. Ray tracing of penetrating radiation showed that the estimated worst case dose is 15.6 krads aluminum equivalent (including a factor of two margin) at the upper MCP. The MCP is not susceptible to radiation damage nor will the radiation cause enough background to be of concern. The 15.6 krad dose easily meets the MMS radiation requirements of 30 krad with a factor of two margin. Active electronic components in particular receive estimated doses of only 6.9 krads or less, again including a factor of two margin.

7.2 Electrical System

Figure 27 is a block diagram of the HPCA electrical system. The gray-accented areas represent individual boards in the electronics unit as well as optical system components. Heavier red lines in the ESA and TOFA indicate particle paths rather than electrical connections. Details of each board and subsystem are discussed in this section.

7.2.1 Command and Data Handling

HPCA's command and data handling (C&DH) subsystem (Fig. 28) provides interfaces to the Central Instrument Data Processor (CIDP). The primary tasks of the HPCA C&DH, which

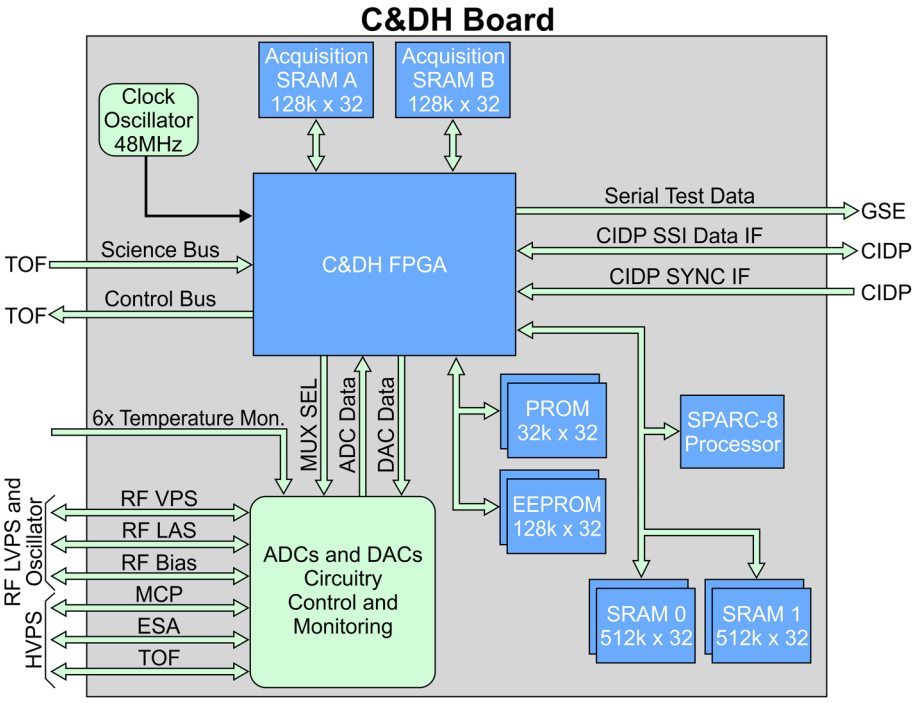

Fig. 28 Block diagram of the C&DH board showing interfaces to the other subsystems

is based on an ACTEL RTAX2000 FPGA, are to control science modes, acquire data from the TOF FPGA, compress and format that data, and transmit the result to the CIDP. Once a command is received ESA energy sweep cycles are executed by commanding HV power supply voltages step-by-step through a pre-loaded 64-step table. Nominally the steps are spaced 625 ms apart. However, in order to deal with possible changes in spin rate, the table also controls the duration of each energy step. The second major task is collection of raw TOF data once every energy step in synchronization with HV sweeps. Data are stored in two ping-pong memories (Fig. 28) and then decimated as required using a process discussed in detail in Sect. 8.3.

Partially decimated data are transmitted to an Atmel SPARC-8 micro-controller that further decimates and compresses science data before passing it back to the C&DH FPGA. The amount of decimation depends on the data mode and is controlled by command. During calibration raw data rates are ~27 Mbps. In Fast Survey Burst Mode this is compressed to 180 kbps (10^3 bits/s) and in Fast Survey the data are further decimated to 5.6 kbps. In Slow Survey data are heavily decimated to 0.8 kbps. Compression modes and their application are discussed in more detail in Sect. 8.3. After formatting the data to CCSDS (Consultative Committee for Space Data Systems) standards, the C&DH transmits it to the CIDP. Figure 29 shows a schematic diagram of the raw data products leaving the HPCA headed for the CIDP or, during ground tests, the instrument EGSE (Electrical Ground Support Equipment).

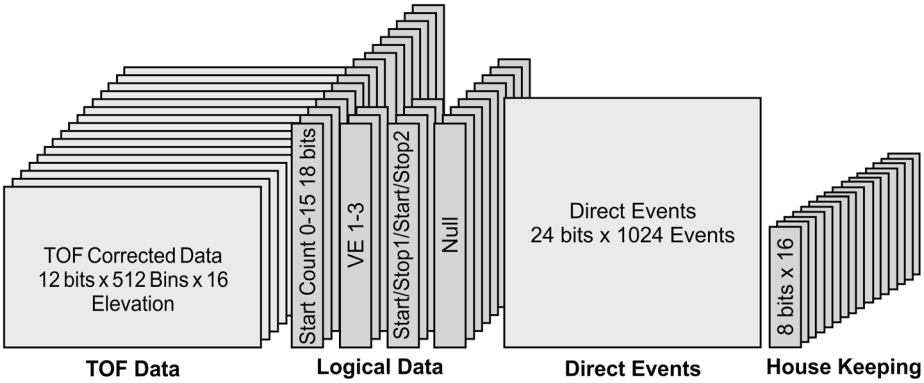

Fig. 29 Schematic of data products produced during Fast Survey mode. In Burst mode the data rate is 180 kbits/s

7.2.2 Time-of-Flight

Much of the TOFA functionality was discussed in Sect. 6.2.2. This section presents details about implementation of the electronics (refer to the block diagram in Fig. 17).

Twenty-four discrete amplifiers and discriminators would have been needed for conventional position encoding methods, which would run up against both volume and power limitations. Our delay line solution discussed earlier requires only 4 low-power amplifiers and discriminators. The former are mounted on the anode board while the latter are located in the TOF ASICs (Figures 17 and 18).

Aliveness and functionality tests of the TOF board are carried out with four built-in pulsers capable of stimulating the anodes and signal chain at rates between 24 kHz and 6 MHz. Pulse amplitudes can be varied as can delays between pulses at intervals of 40 ns to produce an artificial TOF spectrum. Stimulation of all start and stop positions constitutes a complete test of the integrated TOF system.

In addition to science data in the form of ion TOF and elevation and radial positions, the TOF FPGA transmits the number of single events (Start_1, Start_2, Stop_1, Stop_2), valid events for each of the three TOF chips, and the number of times the FPGA state machine was initiated. "Ground truth" data used to check TOF processing is provided by recording the last 1024 valid "direct events" per sample. Direct-event data consist of TOF1, TOF2 and TOF3 values for individual events. These can be checked against the processed position and TOF measurements.

7.2.3 Power System

Figure 30 is a block diagram of the entire power system. Figure 14 is a diagram of the HV distribution network inside the sensor. The power system is comprised of five circuit boards. Moving from top to bottom of the electronics compartment (see also Fig. 4).

- PCB 1: dual-range ESA HV stepping supply; TOF, MCP1 and MCP2 HV supplies
- PCB 2: DC low voltage power supply
- PCB 3: RF low voltage power supply
- PCB 4: RF generator
- PCB 5: RF network (located inside the ESA structure)

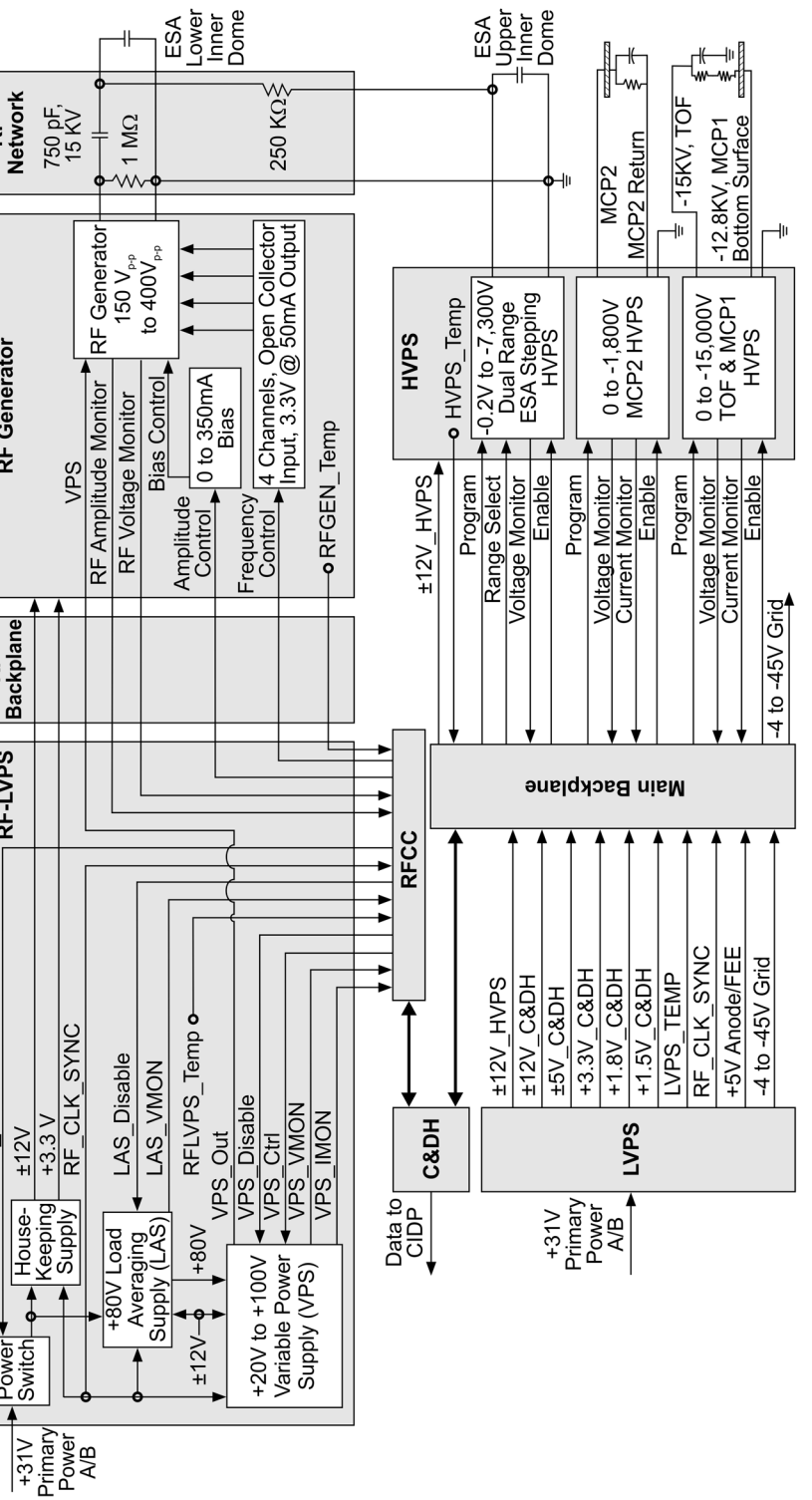

Fig. 30 Schematic of the HPCA power system

Table 5 Summary of HVPS performance

Supply	Output Voltage	Control (Bits)	Peak Output Current	Accuracy (Full Scale)	Full Scale Pk. to Pk. Ripple
ESA Low	−0.21 V to −70.28 V	12	2 mA	±0.003 %	0.01 %
High	−70.28 V to −7000 V			±0.001 %	
TOFA Top	−15.0 kV	12	−45 μA	±0.01 %	0.00 %
TOFA Bottom	−12.75 kV tap from −15 kV supply	None–scales with TOFA −15 KV	−45 μA	±0.01 %	0.00 %
Bottom MCP	−1.8 kV	12	−225 μA	±0.01 %	0.00 %

The RF coupling circuit (RFCC) is a small board that carries RF control and monitor lines. It also acts as a front plane between the C&DH board and the RF-LVPS. Some of the signals in the RFCC circuit run between the C&DH board and RF Generator. For that reason they are routed through the RF_LVPS and RF backplane to the RF Generator.

Low Voltage Power Supply (LVPS) Power lines from the CIDP provide the LVPS with nominal +31 VDC (volts DC) via two redundant lines. The LVPS then converts primary power into eleven secondary voltages needed by the various subsystems (counting ± VDC as two voltages). The primary power is isolated from secondary power through a transformer.

The LVPS is comprised of voltage converters 1 and 2. Converter 1 is a fly-back topology operating at a 200 kHz switching frequency. It produces two sets of ±12 VDC outputs (one each for the HVPS and C&DH boards) and a programmable voltage from 0 to −50 VDC (for the Anode Grid). Converter 2, also a fly-back topology, produces two +3.3 VDC outputs (for the C&DH and TOF boards), and two +5 VDC outputs (for the TOF and FEE boards). Four other voltages are generated for low dropout regulators from the various low voltage supplies. The switch-mode converters used in the LVPS are synchronized to other converters in the electronics compartment. The overall LVPS efficiency is approximately 66 % due to the use of linear regulators and production of many relatively low voltages.

High Voltage Power Supplies (HVPS) Figure 14 shows the network distributing HV to the sensor. High voltage ESA, TOFA and MCP supplies are controlled with signals from the C&DH via the central backplane (Fig. 30). The high voltage multiplier strings in the supplies limit efficiencies to 50 % to 60 %. Table 5 summarizes the performance of the four HV supplies based on measurements with components selected at the time of final pre-integration tests.

Requirements on the ESA voltage levels are set by the range of energies to be covered and by the analyzer constant (Eq. (13)). If the upper energy limit is $E_{\max}$ then the voltage required at the center of the highest energy passband is given by

$$V_{\max} = E_{\max}(1 - \Delta E/2E)/k. \tag{34}$$

Using the ESA analyzer constant $k = 5.45$ derived from simulations and prototype measurements, setting $E_{\max} = 40.0$ keV, and taking $\Delta E/E = 0.091$ at FWHM (obtained from simulation and prototype measurements) gives $V_{\max} = -6936$ V for the highest voltage step.

A similar procedure gives the lowest voltage step for 1 eV ions, $V_{\min} = -0.187$ V, corresponding to 1 eV. For technical reasons the lowest voltage step is -0.21 V ($E_0 = 1.14$ eV) while the upper voltage limit was set at -7000 V.

The HV supplies share several important features. The first is a provision for operating in a divide-by-ten (V/10) mode in which all high voltages are limited to 10 % of their nominal values. The V/10 mode allows supplies to be safely commanded and operated at atmospheric pressure during bench tests and final checkout on the spacecraft. A second provision is HV enable/disable functionality controlled by the C&DH. This promotes instrument safety by forcing the operator to make a conscious decision to bring up high voltage. All of the supplies are controlled by 12-bit DACs. The supplies themselves output 0.0 V to -4.5 V to analog monitors that are digitized and reported in telemetry once per 625 ms sample. In particular this feature is used to monitor the ESA stepping voltage at each point in the scan in order to verify that ion energy is being measured accurately.

The ESA HV supply is a two-part system comprised of driver and voltage multiplier sections together with a stepping control section. In order to achieve the precision required for the ESA the supply is dual range. The low range covers -0.21 V to -70.28 V while the high range covers -70.28 V to -6936 V. In any given scan mode switching from one range to the next is seamless. The accuracy of ESA voltages is ± 0.001 % of the top step value. This translates into the same accuracy in ion energy measurements. The ESA nominally covers the 1 eV to 40 keV energy range using 63 log-spaced steps (Sect. 6.1.2) plus a 64th step that gives the supply time to fly back from the highest to lowest voltage. In order to keep an even cadence of 64 steps per 625 ms, the supply switches voltages from step to step in settling times that vary from 0.500 ms to 19.770 ms depending on the size of the step.

High voltage to the TOFA optics is provided by a programmable supply controlled by a 12-bit DAC. The primary output voltage is -15.0 kV. In addition -12.75 kV is provided by a tap on the multiplier string (Fig. 14) to establish the electric field needed for electron focusing and to provide the correct bias voltage to the upper MCP.

RF Low Voltage Supply and RF Generator The RF LVPS receives power via separate redundant +31 VDC lines from the CIDP (Fig. 30). Having separate LV power for the RF system isolates it from the rest of the instrument and spacecraft electronics. Further isolation is provided by partitioning the two RF boards from the rest of the electronics enclosure and introducing a separate communications backplane.

An important feature of the RF generator is a load-averaging supply that outputs nominal +80 V DC to feed the variable voltage supply needed by the RF Generator. The load-averaging supply has large storage capacitance that can deliver the significant amount of power needed during the RF duty cycle. The latter covers 22 % of the normal ESA sweep period corresponding to the 14 RF energy steps in Table 4.

The RF generator is a high-power RF oscillator whose resonant frequency is controlled by the series resonance of an inductance formed by a ferrite core toroidal transformer and a selectable capacitance. The capacitance consists of a static parasitic component made up primarily of the ESA domes and power cables plus an additional four capacitors that are switched to select the RF oscillation frequency. The capacitors are scaled in a pseudo-binary fashion to yield 16 different frequencies between 5.5 and 9.9 MHz (Table 4). The transformer provides the highest frequency when no capacitors are switched in. Adding capacitors lowers the frequency but increases power dissipation due to the increase in RF current. However the supply is designed such that the extra capacitors needed for the lowest frequencies are used in lower peak-to-peak voltage range, thus minimizing the amount of power dissipated by the RF supply to an average $\sim$4.3 W.

The RF output voltage is carried by a low-capacitance cable to the RF distribution network located inside the ESA inner shell (Figs. 14 and 30). This network couples the ESA DC stepping voltage to the upper inner dome while also coupling the RF voltage to the DC voltage going to the lower inner dome (Fig. 5). There is less than 1 % parasitic coupling of RF voltage from the lower to the upper inner dome so incoming ion trajectories are not disturbed by the RF field nor, in combination with the collimator grid, does RF escape the instrument.

An important feature of the RF design is a structural geometry that effectively forms a Faraday shield to protect the signal electronics from RF pickup. The RF is hundreds to thousands of times larger than the analog detector signals which would otherwise be overwhelmed. The shield is made up of the grounded MCP housing and a capacitively bypassed grid placed between the lower MCP and the anode. During tests with the RF system operating no pickup was detected by the HPCA's very sensitive low-level signal electronics. Moreover the HPCA passed all environmental tests and met all of the very stringent mission electromagnetic interference requirements.

8 Operation

8.1 Instrument Operation

8.1.1 Sample Timing

Data sampling is designed to obtain even coverage of the entire sky (4π sr) in 10 s. Timing, pixel resolution and coverage were discussed in Sect. 4 and summarized in Table 2. Those considerations also determine the rate at which full resolution data are generated [16 (azimuthal) $\times$ 16 (elevation) $\times$ 64 (energy) $\times$ 5 (ion species + background) = 81,920 data words per 10 s]. In fact the actual internal data rates, which include transfer of three sets of TOF spectra binned into 512 samples every 625 ms, are over a thousand times faster.

Acquisition of azimuthal samples is not synced to the spacecraft rotation period. HPCA stepping is allowed to free-run and, since the spacecraft spin rate varies little from 3 rpm, there is little effect on velocity distribution sampling. The slight shift in look directions caused by variation in spacecraft spin rate can be removed easily during data analysis.

Each voltage (or equivalently energy) step involves a number of actions by the C&DH FPGA which (1) sets ESA and RF power supply voltage levels and RF frequency based on pre-programmed tables, (2) waits for ESA voltages to settle, and (3) directs the TOFA electronics to collect TOF and singles data for each step. At each step TOF data from the previous step are sent from the TOFA FPGA to the C&DH FPGA. During Step 0 the ESA HV slews from high to low voltage and any data generated during that step is not saved.

During each energy scan a data set consisting of 63 TOF spectra $\times$ 512 TOF bins $\times$ 16 elevations is accumulated and histogrammed. The resulting TOF spectra are then parsed into five bins that define the ion species H^+, He^{++}, He^+, O^+ and background (Fig. 20). The red portions of the spectrum in Fig. 20 indicate typical species boundaries. Since ion times-of-flight are both mass and energy dependent the range of TOF limits for each species changes with energy (Fig. 31).

8.1.2 Operational Modes

Figure 32 is a high-level schematic of HPCA flight software (FSW) and operations including the ground system discussed in Sect. 8.4.

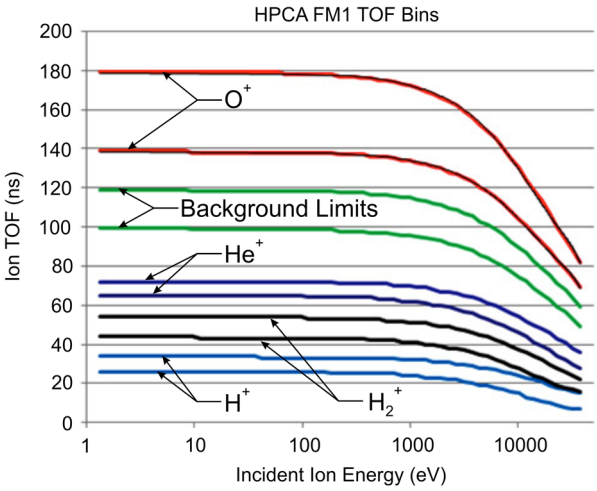

Fig. 31 TOF boundaries as a function of energy for four ion species plus background

When power is first applied, the HPCA goes into a "Boot" state using software stored in PROM. If the instrument passes software self-tests then it proceeds into a "Safe" state running under science mode software stored in EEPROM. At this point the instrument can be commanded out of Safe mode and into a mode in which high voltages can be enabled. With high voltage enabled and applied, if a self-protect mode is triggered by an incident such as excessively high counting rates, or a watchdog reset event occurs (e.g., no command arrives from the CIDP for 30 s), then the instrument will immediately return to Safe State and protect itself by setting all HV supplies to zero volts in a few seconds. It then reverts to the Boot State to await further instructions.

The instrument can only enter the HV-enabled state by telecommand. From this point on the HPCA is fully functional and ESA, TOFA, MCP and RF supplies can be operated using a selection of tables stored in memory. The TOFA and C&DH subsystems are also operational and science and housekeeping data can be collected, formatted and transmitted. The source of low voltage power to the RF supply is controlled separately by the CIDP. HPCA cannot command on the RF LVPS power directly, but does control the LVPS output levels once the CIDP switch is on.

Science modes are defined by setting the range of ESA voltages to be scanned and the science data products to be returned. The voltage scans are table-driven and just about any combination of voltages (i.e., ion energies) can be selected. For example, instead of using the standard 63 log-spaced stepping intervals, linear scans or scans in which only every other log-spaced step is scanned are all possible subject only to limitations imposed by the ESA power supply slew rates.

On orbit HPCA collects and transmits data according to spacecraft position in the orbit and the modes agreed to by the MMS science team. As discussed in Sect. 7.2.1, the HPCA generates three distinct data sets: Slow Survey, Fast Survey, and Burst. Slow Survey data are highly compressed, Fast Survey Data are much less compressed, and Burst Data are minimally compressed. Survey data products are automatically transmitted to the ground. Burst data (only collected during Fast Survey mode) are stored in the CIDP.

Once on the ground, data taken during the previous orbit are examined in order to select a stored subset for transmission to the Science Operations Center (SOC). For this purpose all instruments, including the HPCA, generate "trigger" data in addition to Fast Survey data. Burst data are stored for approximately one orbit and, if not specially marked, are purged

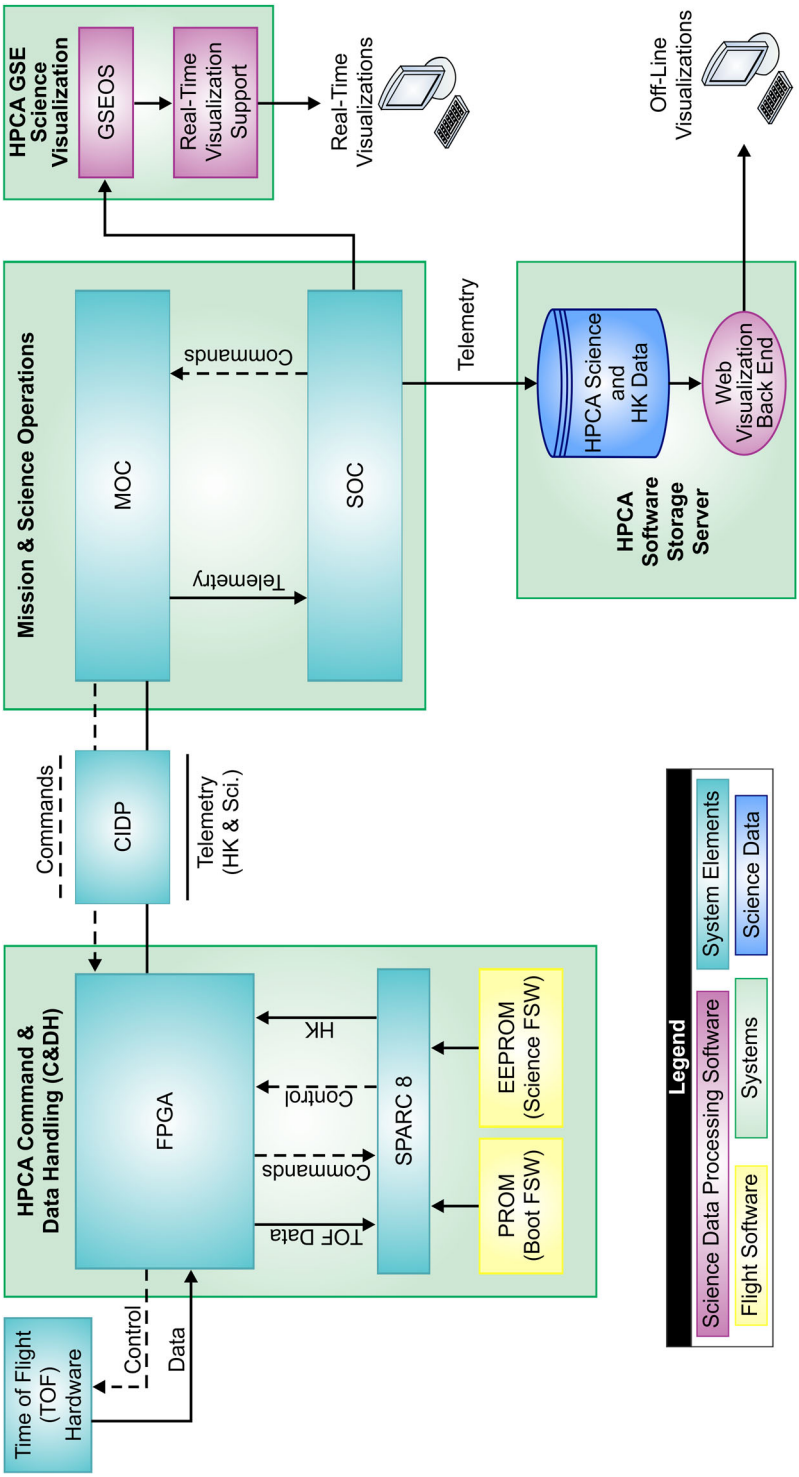

Fig. 32 High level block diagram of the HPCA FSW system illustrating its relation to the CIDP, the Mission Operation Center (MOC), the Science Operations Center (SOC) and the HPCA ground system

Table 6 Science downlink data rate allocations

Mode	% of Time Operated	% of HPCA Data Transmitted	Data Allocation Rate	Daily Allocation
Slow Survey	~50 %	7.4 %	0.8 kbit/s	~34 Mbit
Fast Survey	~50 %	51.3 %	5.6 kbit/s	236 Mbit
Fast Survey (Burst)	1.25 %	41.3 %	180 kbit/s	~190 Mbit
TOTAL	100 %	100 %	N/A	~460 Mbit

from the CIDP to allow new data to be recorded. The duration of selected burst intervals can range from 20 s (one spin) up to the full burst period allocated to any given orbit, approximately 17 minutes. Once an interval is selected, the full HPCA data set is transmitted by the CIDP to the ground at a rate of 180 kbits/s. Regardless of whether or not the data are transmitted to the CIDP, HPCA continues data collection according to its current mode. Data volumes by mode are listed in Table 6.

An important feature of the software is that it will autonomously safe the instrument in case of higher than expected detector counting rates. This situation can occur because of failure of the dynamic range control system (e.g., RF operation) or to arcing in the HV electronics. When high rates are detected the software averages the counting rates to make sure the incident is not due to anomalous data, and then commands the MCP voltage down by one or more steps depending on how the safing procedure is set up. Figure 33 demonstrates the operation of this feature during beam tests. In this case the beam current was raised to a level such that the auto turn-down software detected the high rates. At that point the voltage on the MCP was lowered within a few seconds. After a commanded delay period to let the situation settle (for example to let the spacecraft exit a high flux region) the voltage was automatically raised to normal operating levels and then the test was repeated.

There are several other operational modes designed for specific events that do not involve science, including calibration and maneuver modes. The standard calibration mode generally operates following spacecraft exit from the Fast Survey portion of the orbit in coordination with other particle instruments such as DIS.

8.2 On-Board Data Processing

The TOF measurement process was described in Sect. 6.2.2 and sample timing in Sect. 8.1.1. This section discusses data processing from the operational point of view including what happens once data reaches the C&DH system.

Fast Survey mode is the worst-case data volume and processing load that the system must handle to generate both Fast Survey and Burst data products. Figure 29 represents the raw data products contained in each sample taken during a single energy step. Slow Survey data products are a subset of the Fast Survey products.

The command sequence needed to enter Fast Survey is received by the C&DH from the CIDP and passed to the SPARC-8 processor via the FPGA registers (Fig. 28). The flight software reads and executes the commands, performs any final FPGA and software configuration activities, and then switches to Fast Survey mode. Before data acquisition begins the FPGA transmits the necessary configuration settings to the TOF subsystem based on configuration settings stored in EEPROM. Because only infrequent changes are anticipated to most of the configuration settings, the normal way to adjust instrument behavior will be to upload new configuration tables. New table values will be applied the next time science operations are initiated.

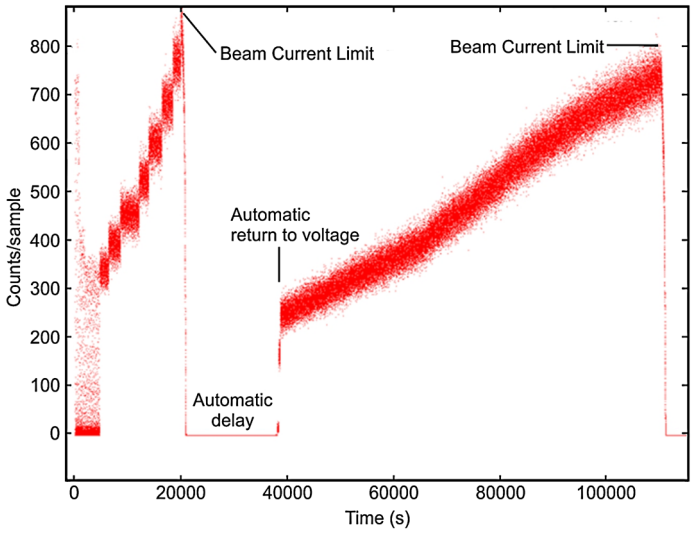

Fig. 33 Demonstration of the MCP protection feedback loop using the EPIC ion beam. Data were taken with FM1 over a period of approximately 33 minutes. The beam current limit was set by telecommand as were the automatic delays

Science data processing is divided into three distinct parts (Fig. 28). Part 1 is the high-speed pipeline which controls TOF data collection, reads raw data from the TOF board into the FPGA, performs primary data decimation in the FPGA, reads the partially decimated data into the SPARC-8 memory, and performs secondary decimation in FSW. The handoff of the data between the FPGA and the FSW uses the science data acquisition ping/pong memory. Operations are synchronized such that the FPGA is writing into one-half of the memory while the SPARC-8 is reading from the other half.

Part 2 consists of a sequence of operations performed on each data product as it becomes available (rather than holding data in the pipeline) and generates each science data message sent to the CIDP. The rate at which these data are processed is determined by decimation factors set by ground command. At the highest rate, Part 2 processing may occur more frequently than once per azimuthal sample (625 ms). Once a set of decimated data is available to the software (based on currently selected decimation factors), the Part 1 pipeline is directed to a second data buffer in the SPARC-8 memory, and data in the first memory are then processed (Part 2 processing). This second step consists of performing lossy compression and recomposing the data for subsequent operations. The next stage is lossless compression, which ends with the data ready for inclusion in a CCSDS packet together with housekeeping information and check sums. In Part 3 of the process the completed packet is handed back to the FPGA for transmission to the CIDP.

8.3 On-Board Data Decimation and Compression

Depending on the desired telemetry rate, data are decimated by co-adding over the appropriate parameters such as elevation, azimuth and energy bins. The extent of decimation is set by parameters that determine the number of elements of each parameter to be summed. For example adjacent elevation channels may be summed together two, four, or eight at a time. Likewise adjacent energy steps or azimuthal sectors may be summed together any number

of times so long as the number is binary. The summations of course degrade velocity space pixel resolution but still permit equally spaced samples and comparable smearing of all three velocity distribution elements.

The decimation process is distributed between the FPGA and the flight software running in the SPARC-8. Since the TOF and elevation spectra arrive every sample they are summed in the FPGA. Energy and azimuth sampling is much slower so the arrays can be summed in the SPARC-8 by the flight software.

Following decimation, data products are organized into packets that are compressed by a factor of two by the FSW. Two compression methods are used. First, the (decimated) number of counts in the TOF histogram is summed over the counts corresponding to the four ion species and background. These and the logical data products are reduced from 32 to 16 bits using a lossy logarithmic compression technique.

After lossy compression, lossless (Rice method) compression is applied to the data. Some small products (e.g., trigger data) are not compressed. Compressed data are combined with non-compressible data (such as time stamps) and formed into CCSDS telemetry packets ready for transmission to the CIDP (Fig. 28). The C&DH FSW interleaves the science telemetry packets with housekeeping, heartbeat, trigger data, and other packets generated by the FSW such that whole messages are transmitted to the CIDP.

The most highly compressed science data generated by the HPCA is the trigger number set which is used by the MMS team members at the SOC to determine whether data taken during a particular burst period should be transmitted to the ground. Since the amount of burst data that can be transmitted is severely limited (compared to the amount generated during an entire orbit) the trigger number has been carefully selected to give only the most essential information produced by HPCA. That value is a weighted average of the plasma composition given by

$$\mathrm{TRIG} = \Sigma_1^4(\alpha_i M_i C_i)/\Sigma_1^4(C_i) \tag{35}$$

where α_i is a species-dependent scaling factor, i is the species index ($i = 1 = \mathrm{H}^+$, $i = 2 = \mathrm{He}^{++}$, $i = 3 = \mathrm{He}^+$, $i = 4 = \mathrm{O}^+$), M_i is ion mass/charge, and C_i is the number of counts per species. One trigger number is generated for each azimuthal sample (16 per 1/2 spin).

One last data stream to be discussed is used only during ground activities when the instrument is connected to the Electrical Ground Support Equipment (EGSE; see Sect. 9.1), primarily during calibration. The stream is very high rate (~27 Mbit/s) and is transmitted directly from the C&DH to the EGSE. The stream does not go through the much slower CIDP connection and hence is available only during ground test. Its purpose is to extract every piece of data generated by the HPCA at full resolution in order to diagnose and calibrate performance in full detail.

With high-speed data it is possible to calibrate the instrument and to check all functionality. In parallel the normal Fast Survey stream including burst data is also generated and collected. Subsequent analysis and verification can then be carried out by comparing the all-inclusive high-speed data with compressed science data sent via the CIDP simulator included in the EGSE.

8.4 Ground Operations

8.4.1 Commanding

During flight operations instrument commands are generated at SwRI and then verified by running the command sequences on the HPCA Engineering Model (Fig. 34). Commands are then sent to the SOC for uplink and executed out of a time-tagged sequence run on board the spacecraft. Other than during commissioning no real-time operations are required.

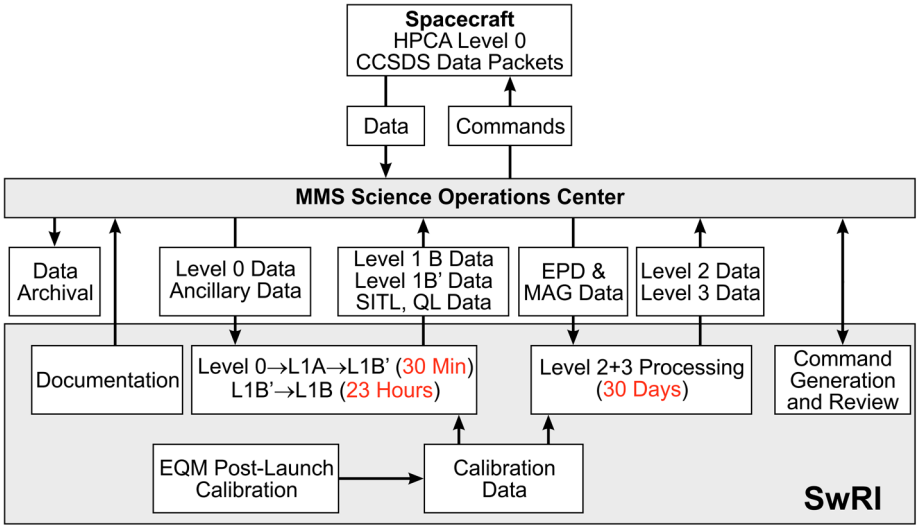

Fig. 34 Schematic of the HPCA ground system showing the production and exchange between the SOC and SwRI of Level 0 through Level 3 data

8.4.2 Data Processing

Figure 34 shows more detail of the ground system and operations. Raw (Level 0) science data arrive at the MMS SOC from NASA ground stations and are streamed from there to SwRI within 30 minutes of receipt. Within another 30 minutes these data are processed automatically by HPCA ground system software into a form that provides the scientists located at the SOC with Level 1B′ data suitable for quick perusal that allows choice of the burst periods to be down-linked on the next spacecraft pass. More complete, but still uncalibrated "quick-look" data (Level 1B), are delivered by SwRI to the SOC within 23 hours of the first receipt of data. Intermediate products, termed Level 1A, are used to produce higher order data products but are not themselves delivered outside SwRI. All Level 1 data are produced with a cadence of 10 s.

Calibration factors are applied to Level 1B data to generate Level 2 products that consist of physical parameters such as velocity distribution functions and moments such as density, flow velocity and temperature for all four ion species. These are provided on the highest available time resolution: 10 s for 3-dimensional parameters such as velocity and 625 ms for 2-D snapshots of elevation, energy, and mass. The final step in data production is Level 3 where the in situ magnetic field and similar auxiliary data are used to derive parameters such as pitch angle distributions, plasma beta, and the Alfven velocity. Additional products such as synthesized energy spectra can be obtained by combining HPCA data (at energies $<$40 keV) with Energetic Particle Detector (EPD) data above that energy. Both Level 2 and 3 data sets will be delivered to the SOC within 30 days.

The bottom of Fig. 34 indicates that additional calibration data may be taken with the HPCA Engineering Qualification Model (EQM), which has been reworked to be as nearly identical to the flight models as possible—particularly in the critical area of the RF generator, the anodes, and the TOF electronics. The reason for upgrading the EQM to flight performance levels is that it could well be required in case unusual phenomena are encoun-

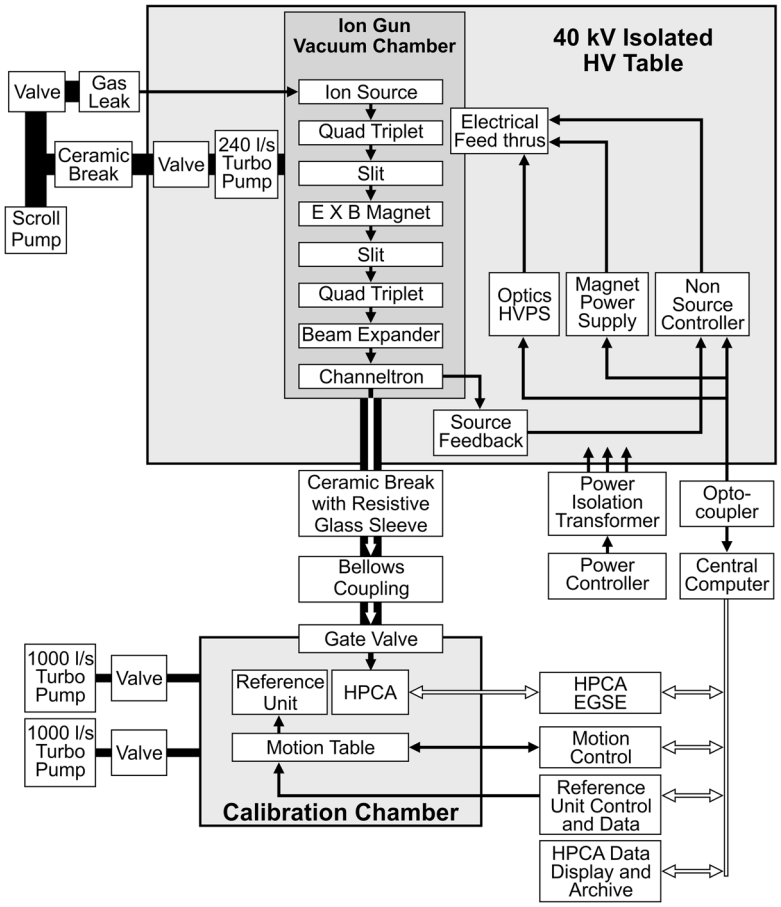

Fig. 35 Schematic diagram of the EPIC calibration system. *Red arrows* linking the optical elements within the Ion Gun Vacuum Chamber indicate the path of the ion beam. All other *arrows* indicate electrical connections or data flow

tered outside the anticipated normal range of performance. One example would be unusually high and rapidly varying ion fluxes that exceed dynamic range capabilities.

9 Calibration System

9.1 Introduction

Because of its complexity the HPCA is a very demanding instrument to calibrate (see Wuest et al. 2007 for an excellent discussion of particle instrument calibration). For this reason, and because four separate units had to be calibrated over a long period of time including EQM calibration post-launch, we built a dedicated calibration system incorporating several novel elements including a compact ion source and ion beam generating optics, and a highly accurate system used to calibrate the beam itself. Figure 35 is a diagram showing the overall layout and major subsystems of the Energetic Plasma Ion Calibration (EPIC) facility. Key

features of the system include the Calibration Chamber in which the instrument and a Calibration Reference Unit are housed, an Ion Gun and associated beam formation optics, a high voltage enclosure that isolates the ion gun and optics at potentials up to 40 kV, and a control system that operates the calibration elements in synchrony with the HPCA instrument.

An important component of the calibration system is the HPCA's Electrical Ground Support Equipment (EGSE), which acts as a power source, control system, and data collection and processing system. Although it supports ordinary engineering tests, once the EGSE is synchronized with the EPIC facility electronics the two coordinate facility functions with HPCA operations. For example, once the calibration system positions HPCA in the correct orientation with respect to the incoming ion beam, the pre-selected instrument measurement cycle commences automatically. After data are taken they are transferred to a central display and archival computer along with ancillary calibration data. Then the next run is set up and the procedure continues until a measurement cycle (e.g. an energy-angle scan) is completed.

There are ten primary instrument performance parameters to be measured and recorded during calibration:

- Center and resolution of azimuthal response,
- Center and resolution of elevation response,
- Center and resolution of energy response,
- Center and resolution of TOF peaks,
- Association of TOF with ion M/q and species,
- Pixel and total sensitivity as a function of energy and ion species.

Following a description of the EPIC system we describe calibration procedures. In Sect. 10 we show calibration results and discuss instrument performance.

9.2 Ion Source and Beam

The calibration system is divided into five main components (Fig. 35): (1) an ion source and associated beam formation optics mounted in an isolated HV enclosure, (2) a motion system that positions and rotates the instrument across the ion beam, (3) a beam Calibration Reference Unit (CRU) mounted on the same platform as the HPCA, (4) an ultra-high vacuum (UHV) chamber and pumps, and (5) a control and data acquisition computer system synced to the HPCA EGSE.

Figure 36 illustrates the components that make up the ion source and beam line optical elements. Figure 37 is a photograph of the beam system.

Once the ion source and beam line are mounted on the optical bench (Fig. 36), the bench is turned upside down and bolted on top of the box-like beam high-vacuum chamber running from lower left to upper right in the photograph (Fig. 37). This gives easy access to the beam line for changing source filaments.

With reference to Fig. 38, which shows ion trajectories moving from left to right, the principal optical elements are:

- Electron bombardment ion source and a series of focusing and accelerating lenses that form the initial beam (source lenses are not shown).
- A series of three quadrupole lenses (Q1 through Q3) that shape and rotate the beam prior to the $E \times B$ Wien filter.
- X- and Y-focusing plates (not shown) that align the beam with the $E \times B$ filter.
- Aperture lenses BC1, B, and BC2 that match the beam cross-section to the shape of the $E \times B$ filter aperture.

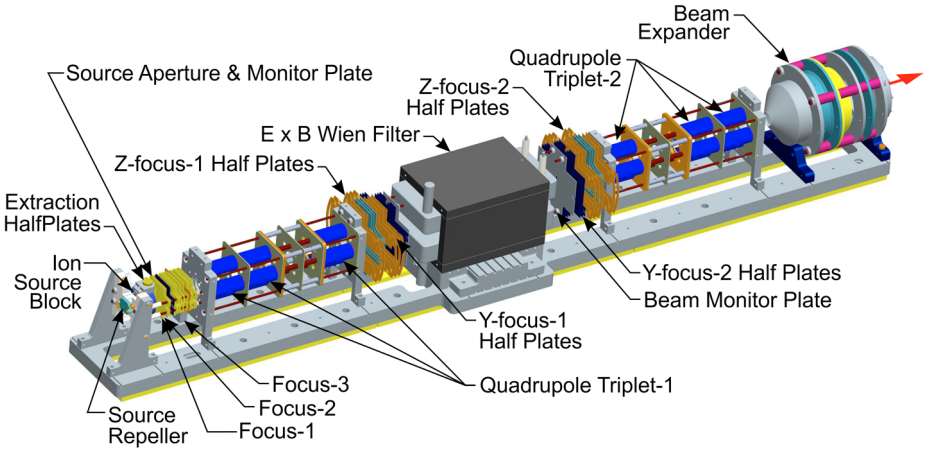

Fig. 36 Graphic depicting the EPIC ion source and ion beam system

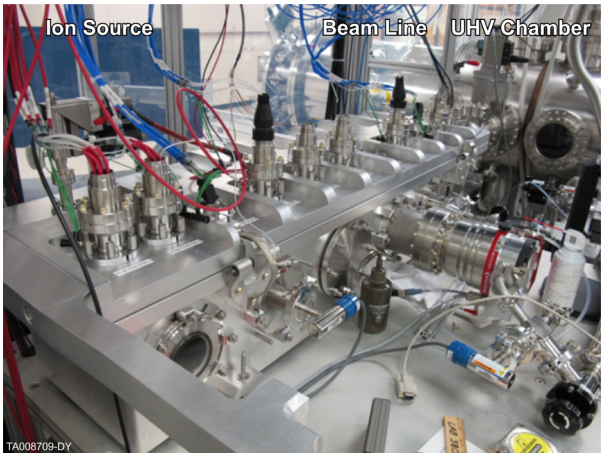

Fig. 37 Photograph of the ion source, beam line, and UHV calibration chamber

- An $E \times B$ Wien velocity filter that uses an electromagnet to select ion species. A set of E-field correction shims within the Wien filter help reduce aberrations that tend to defocus the beam.
- A second set of quadrupole lenses Q4 through Q6 that reshape the beam for the final element.
- Point-to-parallel beam expansion optics (EXPN) that center and shape the beam to match the HPCA aperture.

The ion source is located at the far left in Fig. 38. The upper panel is a view of trajectories travelling in the vertical plane while the lower panel shows trajectories in the horizontal plane.

One or more gases are leaked into the electron bombardment source where ions are created by a variable ~70 eV electron beam. The ion source block consists of two filament assemblies, the volume where ions are created, and an electron repeller and trap that float on top of, and are referenced to, the ion source block potential. The filament emission current (variable from 0 to 750 μA) is regulated by the filament emission controller that makes use

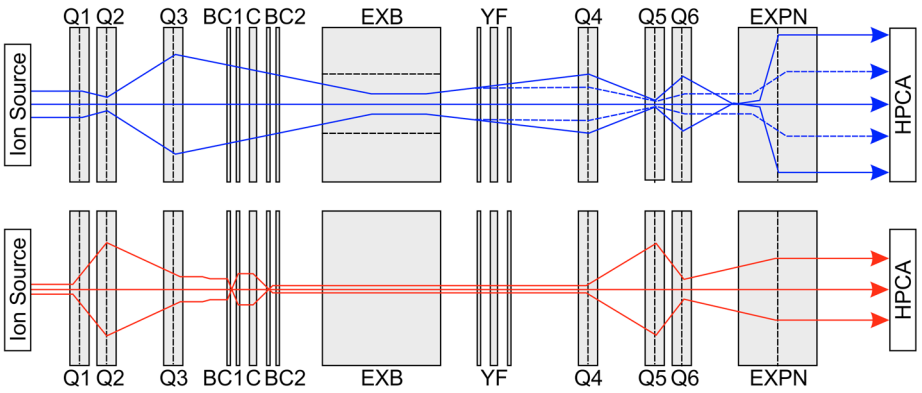

Fig. 38 Schematic of ion trajectories travelling through the ion beam system. *Upper trajectories* are travelling in the vertical plane; *lower trajectories* are in the horizontal plane

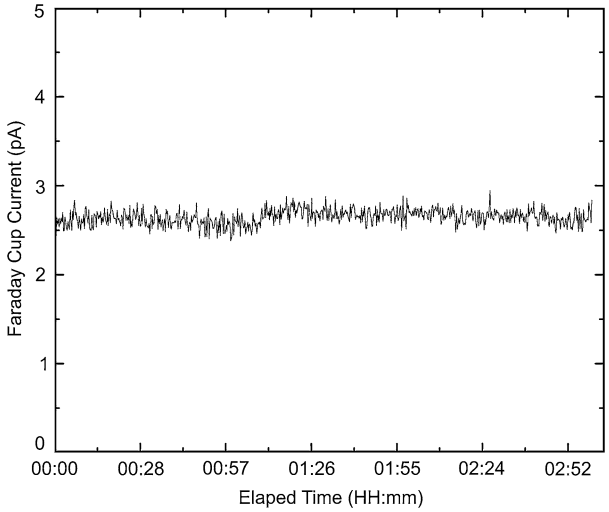

Fig. 39 Ion beam current measured over a period of 3 hours using the EPIC Faraday cup. During this period the ion source was under the control of a feedback loop from the CEM monitor (Fig. 36) to the source controller

of current feedback from the electron trap. The ion source float voltage can be varied with respect to common ground up to +5.0 kV. The float voltage defines the beam accelerating voltage and consequently its energy. The voltage that controls the potential of the Isolated HV Float Table (Fig. 35) is variable from earth ground up to +40 kV which, in combination with the +5.0 kV source accelerating voltage, allows beam energies up to 45 keV. Beam stability is monitored using current collected from a small plate located just downstream of the $E \times B$ filter. Stability measurements show that the beam current is maintained within approximately ±5 % over 3 hours (Fig. 39).

Beam composition is controlled by the choice of gases leaked into the source and by mass/charge selection using the Wien filter. The standard gas sample used in most calibration runs was a mixture of H:He:N:Ne:Ar chosen in such a way that the resulting beam composition was in the ratio 1:1:1:1:1. Since the Wien filter selects for velocity, and the beam leaving the source has a constant known energy, the system selects ion mass/charge by controlling magnet current. With the $E \times B$ filter deactivated the beam carries all five

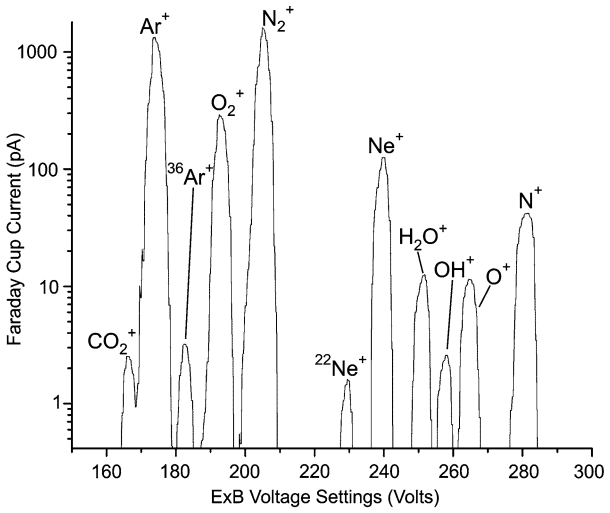

Fig. 40 Mass spectrum taken by scanning the magnet in the $E \times B$ velocity filter

species. With the Wien filter properly tuned the calibration system is capable of mass resolution in excess of $100M/\Delta M$ FWHM (Fig. 40).

Beam parameters are set by voltages and currents controlled and monitored by a dedicated computer. Once they are set up manually, voltage and current settings needed to reproduce an ion beam with specific energy, ion species, cross-section profile, and intensity can be saved in a beam "snapshot" file. When executed later the snapshot file sets the voltages and currents needed to accurately recreate the same set of beam parameters. By saving snapshots any type of beam can be set up quickly and accurately, saving a considerable amount of time during calibration.

9.3 Motion System

HPCA views a wide range of azimuth and elevation directions. Calibration requires that the corresponding angular passbands and their centers be measured. Since ion beams covering all angles simultaneously do not exist, the highly parallel ion beam produced by EPIC is aimed at the center of the instrument aperture while the HPCA is rotated about azimuth and elevation axes centered on the instrument's optical axis (Fig. 13).

Like the ion beam system, the motion system (Fig. 41) is compact, making efficient use of space inside the UHV chamber. The integrated HPCA is mounted on a motion platform that travels along the calibration system Y-axis, which corresponds to the HPCA's optical axis of symmetry. Figure 42 is a photograph of the HPCA mounted on the motion platform prior to positioning the assembly in the UHV chamber. The entire platform can be moved from outside the chamber, where there is easy access for instrument mounting, along the Y-axis to position the instrument or the CRU sensors at the beam center. Figure 42 shows the HPCA mounted on the motion system platform about to be moved into the calibration chamber.

The motion platform can rotate HPCA $\pm 180°$ about the Y-axis, equivalent to a complete scan in elevation, and $\pm 12°$ about the Z-axis, equivalent to a scan across the azimuth FOV (Fig. 41). Both axes have a resolution of better than 0.1°. As the motion platform moves along the Y-axis, the center of rotation moves with it. Thus the apertures of the CRU sensors swing in small arcs when the platform is rotated, requiring corrections to obtain their location.

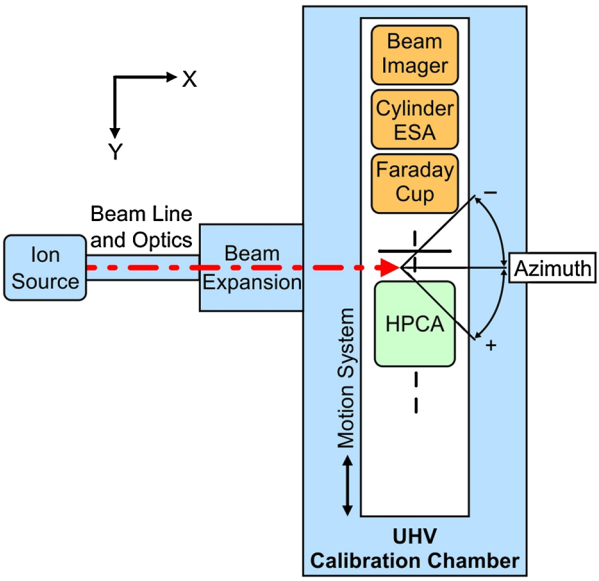

Fig. 41 Block diagram of the EPIC motion system

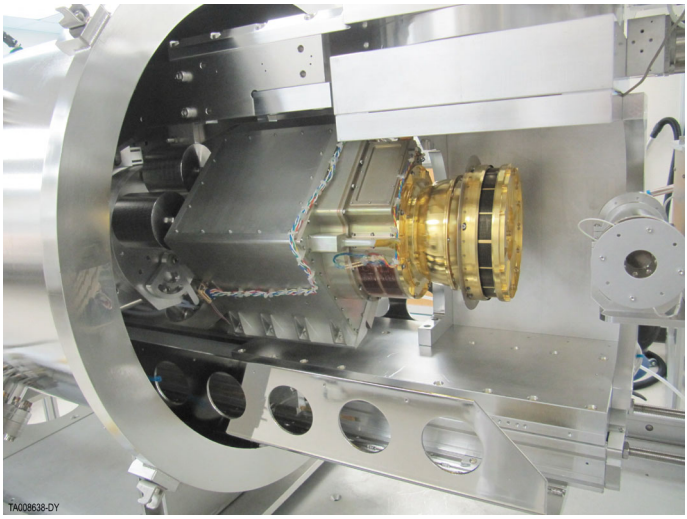

Fig. 42 Photograph of the HPCA mounted on the motion platform about to be moved into the UHV calibration chamber

The beam spread in azimuth is measured by placing the ESA entrance slit at the center of the beam and then rotating the motion platform by an angle α_R to change the beam's angle of incidence at the ESA entrance slit. However, because the ESA slit is offset 251.48 mm from the platform's center of rotation, a correction must be made for its motion in an arc about the center of rotation. The location of the slit is given by

$$Y_{\text{slit}} = X_{\text{ESA}} \cos\alpha_R + Y_{\text{ESA}}(2 - \cos\alpha_R) \text{ [mm]} \tag{36}$$

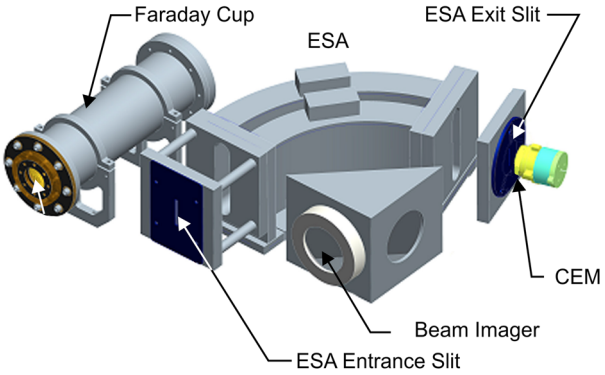

Fig. 43 Three-dimensional drawing of the CRU and sensors

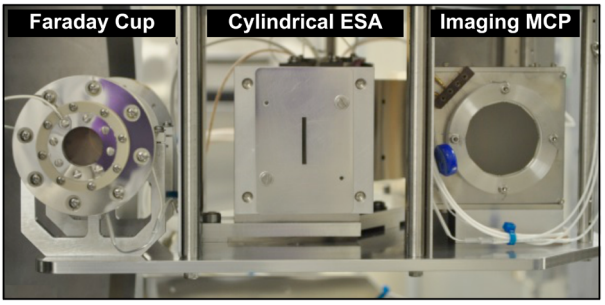

Fig. 44 Photograph of the CRU looking into the sensor apertures

where Y_{slit} in mm is the location of the slit in the calibration coordinate system relative to the rotation center at $(X, Y, Z) = (0, 0, 0)$, and Y_{ESA} is the distance in mm from the ESA aperture to the platform's center of rotation. Similarly, the X-location of the entrance slit in the calibration coordinate system for an azimuthal displacement in mm is

$$X_{\text{slit}} = X_{\text{ESA}} \cos\alpha_R + Y_{\text{ESA}} \sin\alpha_R \text{ [mm]}. \tag{37}$$

By convention, counterclockwise rotation about the Z-axis results in positive azimuthal displacement. Similarly, counterclockwise rotation about the Y-axis (the HPCA symmetry axis) results in positive elevation displacement. In this coordinate system, when the rotational center of the motion system coincides with the nominal beam center the position coordinates are $(X, Y, Z) = (0, 0, 0)$, and angle coordinates are (AZ, EL) = (0°, 0°). Following positioning commands from the central computer the system moves and then settles within a few seconds after which the position is recorded and the HPCA begins to take data.

9.4 Calibration Reference Unit

The Calibration Reference Unit (CRU) consists of a Faraday cup, an ESA, and a beam imager all mounted together on the motion system (Fig. 43). The three measurement techniques fully characterize the ion beam and allow beam parameters to be traced back to calibrated laboratory equipment such as power supplies and pico-ammeters. Figure 44 is a photograph of the three sensors seen from the front. In more detail the CRU sensors include:

- A Faraday cup designed to measure beam currents >0.1 pA.
- A high-resolution cylindrical ESA, which measures beam energy and passband width, the location and width of the beam along the Y-axis, the beam's angle of incidence, and the beam current.

- A beam imager that measures uniformity and location relative to the X- and Y-axes.

The CRU is mounted on the same motion platform as the HPCA, at fixed distance from the rotation axis of the motion system (Fig. 41). During calibration the CRU can be moved accurately into and out of the beam for beam characterization. Beam calibration is alternated with HPCA measurements using snapshot scripts that automatically move the correct CRU sensor into and out of the beam as needed. Beam characterizations are performed every time a calibration run starts and ends, or when the beam composition or energy is changed.

9.4.1 Faraday Cup

The Faraday cup (FC) provides a direct measurement of ion beam current with 100 % efficiency. Going back to the geometric factor equation

$$G \approx A_{\text{eff}} \langle \Delta\alpha \Delta E/E \rangle \Delta\beta \ [\text{cm}^2\,\text{sr}\,\text{keV/keV}] \tag{9}$$

where area and efficiency ε_{ij} are usually lumped together as the "effective" area A_{eff} since it is virtually impossible to measure efficiency separately. This equation delineates the main parameters to be calibrated: A_{eff}, $\langle \Delta\alpha \Delta E/E \rangle$, and $\Delta\beta$.

The effective area is probably the most difficult measurement because it requires a steady ion beam and an accurate current measurement. The relationship between the beam flux F_B and A_{eff} is given by

$$A_{\text{eff}} = C_0/F_B \ [(\text{cts/s})]/[(\text{ions/cm}^2\,\text{s})] \tag{39}$$

where C_0 is the HPCA counting rate in counts/s (cts/s) and beam flux is in units of ions/cm^2 s. Flux is proportional to ion beam current

$$F_B = I_{\text{FC}}/A_{\text{FC}} = 1.99 \times 10^6 I_{\text{FC}} \ [\text{ions/cm}^2\,\text{s}], \tag{40}$$

where FC current is measured in pA. Then

$$A_{\text{eff}} = 5.03 \times 10^{-7} C_0 \ [\text{cts/s}]/I_{\text{FC}} \ [\text{pA}] \ [\text{cm}^2 \ \text{counts/ion}]. \tag{41}$$

The units [counts/ion] reflect the efficiencies (always <1) that go into converting ions to counts. Counting rates need to be $\sim 10^5$ s^{-1} for statistical and engineering reasons. Since the HPCA effective area is $\sim$0.1 cm^2 beam currents need to be $\sim$0.5 pA, which is easily achieved.

At low beam currents the CRU's ESA CEM has to be used to monitor current instead of the FC. Figure 45 is a calibration between FC current and the CEM counting rate, C_{ESA}, giving the relationship

$$I_0 = 1.37 \times 10^{-3} C_{\text{ESA}} - 2.07 \times 10^{-2} \ [\text{pA/cm}^2]. \tag{42}$$

Figure 46 is a plot of ESA CEM counting rate vs. beam current measured by the FC over a wide range of ion species that corresponds to the mass spectrum in Fig. 40. This also demonstrates that the CEM efficiency is very nearly constant with ion mass.

9.4.2 High Resolution CRU ESA

The high resolution CRU ESA is a cylindrical energy analyzer combined with a CEM detector (Fig. 43). The ESA measures all basic beam parameters and their variation along the Y-axis:

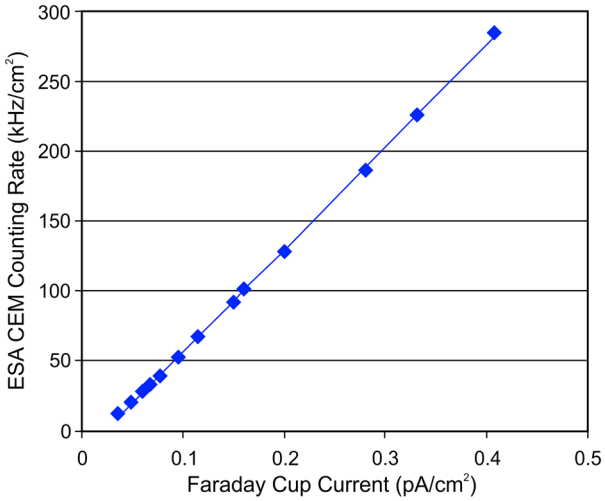

Fig. 45 ESA CEM counting rate plotted as a function of the Faraday cup current

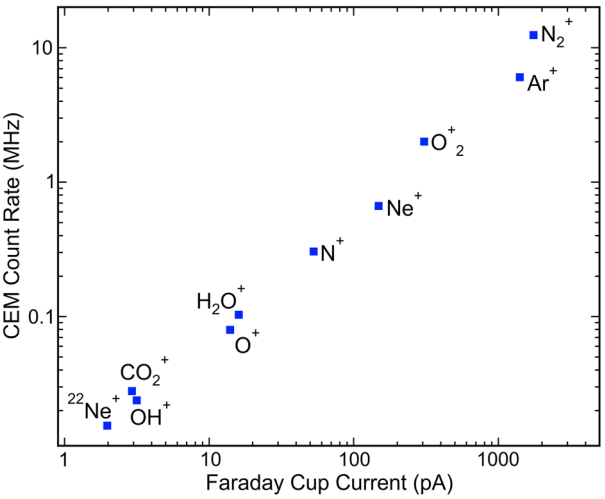

Fig. 46 ESA CEM counting rates plotted as a function of FC current for 10 ion species selected from the mass spectrum in Fig. 40. Going from left to right the species are *not* in order of mass/charge but rather are in order of increasing beam current

- Central energy, energy spread, and energy uniformity
- Azimuthal angle of incidence and angular spread
- Position of beam center and cross-section along the Y-axis
- Counting rate across the beam cross-section.

A cylindrical ESA is used because it is more compact than a spherical ESA and only one-dimensional scans are required. The ESA has a 73.0° bending angle and a central radius of 127.15 mm, giving it excellent beam focusing capabilities, high collection efficiency, and an exact analyzer constant of 5.00. The ESA detector is a Burle series 4800 CEM which can measure beam current densities linearly from as high as 0.5 pA/cm^2 (Fig. 45) to as low as 10^{-3} pA/cm^2.

Balanced voltages $V_1 = -V_2$ are applied to the inner and outer ESA shells to select an ion energy, E_0, which can be calculated from

$$E_0 = k_{\mathrm{ESA}} \Delta V_{\mathrm{ESA}} \ [\mathrm{keV}] \tag{43}$$

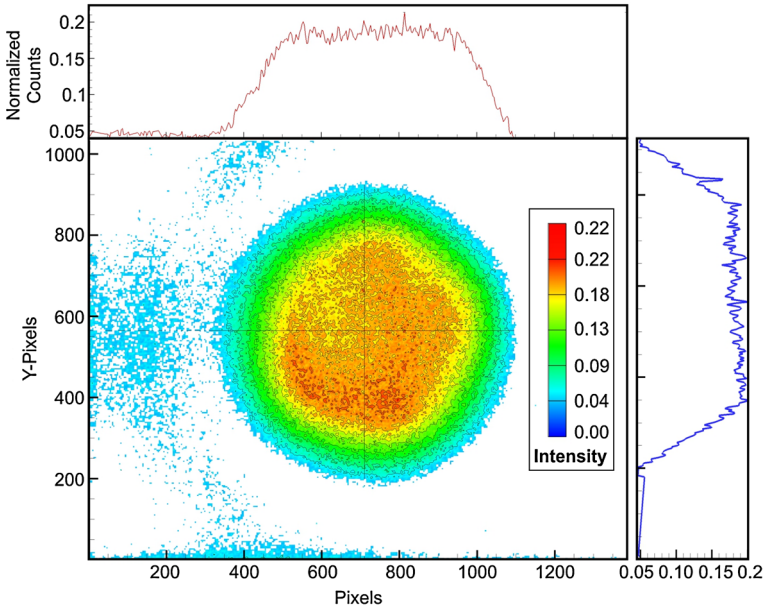

Fig. 47 Image of the ion beam taken with the Beam Imaging Solutions Model 40 (BOS-40). The beam profiles are obtained by summing across the image. Data are normalized to the camera's intensity resolution of 8 bits

where E_0 is the beam energy in keV and $\Delta V_{\mathrm{ESA}} = V_2 + |V_1|$ in kV. The analyzer constant $k_{\mathrm{ESA}} = 5.00$ is obtained from numerical simulations. Beam energy is calibrated by stepping ΔV_{ESA} using a calibrated voltage supply and then taking the centroid of the distribution. The beam spread in azimuth is calibrated using the method described in Sect. 9.3.

9.4.3 Beam Imager

Beam profiling in the $Y-Z$ plane (orthogonal to the beam direction) is made with a commercial Beam Imaging Solutions Beam Observation System Model 40 (BOS-40). The imager's active diameter is 40.0 mm and its center is offset 368 mm from the rotation center of the motion platform. Rotation is not required for measurement since the profile is taken in a plane perpendicular to the beam direction. The imager combines an MCP backed by a phosphor screen. This creates an image that is relayed to the control computer using an image intensified camera located outside the vacuum system. When projected on the EPIC computer monitor the image can be captured to give a detailed record of beam extent and uniformity. An example of a beam image and profile is shown in Fig. 47. The beam is flat across the top with FWFM of 16.0 mm and FWHM of 22 mm. The HPCA collimator entrance is 14.0 mm high, which means that the beam entirely fills the aperture at FWFM.

10 HPCA Calibration

10.1 Introduction

This section describes the methods of calibration and related data analysis. Calibration *in situ* in space in a highly variable environment is virtually impossible although it has been

Table 7 Measurement parameters and required calibration system properties

Measurement	System coverage	Coverage resolution
Effective aperture area	~0.1 to 10 pA/cm^2	N/A
Elevation centers	0°, 22.5°, 45°, . . . ,360°	2° steps
Elevation passband	22.5° FWFM	2° steps
Azimuthal passband	±10° FWFM	1° steps
Mass range	1 to 16 amu	H^+, H_2^+, He^+, O^+
Mass resolution	4 ($M/\Delta M$) FWHM	H^+, H_2^+, He^+, O^+
Energy range & steps	10 eV/q to 40 keV/q	95, 302, 961, 3059, 9741, 33040 eV
Energy resolution	0.17 ($\Delta E/E$) FWHM	$E_0 \pm 0.01 \Delta E/E_0$
TOF range	1 to 250 ns	H^+, $^{40}Ar^+$
MCP gain	$>3 \times 10^6$	Any energy, species, or current
RF passbands	524 to 4259 eV	496, 814, 1337, 2197, 4259 eV
RF transmission species	H^+, He_2^+, He^+, O^+	H^+, H_2^+, He^+, O^+
Dead time	~10^{-13} to 10^{-10} A/cm^2	N/A

tried. Thus calibration must be performed in a ground laboratory with accurate reference standards. The primary goal of calibration is to relate instrument measurements to those made with an accurately defined ion beam of known energy, composition, angular direction, cross-sectional area and intensity.

Because it is impossible to measure every parameter at highest resolution (e.g., every energy and angle step), calibration must be carried out over a sparsely sampled phase space that is nonetheless dense and regular enough to permit interpolation or extrapolation when necessary. Examples include the entire 63-step energy range where there is not enough time to set up a beam at every step. Moreover beam energy of the EPIC system cannot be extended to the lowest energy range <100 eV. Thus simulations play an important role in filling in the missing data points during analysis.

In addition to beam measurements, calibration has other important goals related to HPCA functionality. Primarily these are to verify that HPCA in fact meets all performance requirements in Table 2 and to verify that HPCA meets all engineering requirements such as power consumption, FSW standards, and creation and transmission of data products. Cross-calibration with other MMS instruments is an important goal but is not addressed here.

10.2 Calibration Process

Calibration consists of measuring HPCA counting rates in the various detector channels (Start, Stop, TOF1, etc.) as a function of instrument state parameters (voltages, discrimination levels, etc.) in response to known ion beam parameters (incidence angle, species, energy, current). The relationship between instrument state and beam parameters defines the set of calibration constants. The objective of calibration is to determine those constants.

Based on HPCA performance requirements listed in Table 2 it is possible to define a set of calibration system requirements (Table 7). The only item in the table that might be unclear is the current density requirement for effective aperture area and dead time. Effective area is proportional to the ratio of instrument counting rates to current density (41). Since we want to stay in the range of 10^4 to 10^6 counts/s, in order to measure an effective area ~1 to 0.01 cm^2 counts/ion/s, the beam must provide currents in the range of 0.1 to 10 pA/cm^2.

In addition to the primary calibration constants in Table 7 there are a number of auxiliary parameters to be determined as well. These include, for example, MCP gain as a function of bias voltage, and the performance of the amplifiers and discriminators. Checking that starts, stops and valid-events data match the primary TOF measurements also falls into this category. Calibration system auxiliary data to be collected in coordination with HPCA operations include beam energy, beam current, ion source pressure, and Residual Gas Analyzer (RGA) scans to monitor the composition of background gas in the chamber.

In order to speed up calibration (time = schedule = money), only a limited selection of parameter values were measured, each with approximately the same density of points. Snapshot scripts were used for both beam and instrument settings making calibration as nearly identical as possible from one instrument to the next.

The procedure for performing a calibration step was to set up the ion beam in the appropriate configuration and then capture its characteristics using the CRU. If the beam species was changed from one run to the next then the $E \times B$ filter was swept to establish composition. Once the beam was set up the HPCA ESA was commanded to perform a micro-energy scan in which the ESA energy passband was covered in a series of 64 micro-steps ($\sim$1 % of the passband width) out to $\pm$20 % of the beam center. By micro-stepping the ESA we obtain a detailed energy passband at every calibration point. This is particularly important when characterizing the HPCA's azimuth-energy passband. It is also of interest when covering the elevation passband in order to make certain that there is no cross-coupling between elevation and energy.

When a parameter had to be characterized across the entire energy range we used a selection of seven logarithmically equal-spaced energy steps separated by a factor of approximately three (Table 7). However it still was not possible to sample all of the measurement space (e.g., all angles) even at these few energies so a single energy of 3.159 keV was chosen for most angle samples because it is in the central part of the energy range where the -15 kV acceleration potential still has some effect on ion trajectories. (At very low energies ion trajectories into the TOFA are entirely dominated by the electric field created by -15 kV, while at the highest energies the field has little effect on trajectories.)

11 Calibration Results

Table 8 summarizes calibration results for all four flight models. In this section we will discuss the results, note discrepancies between data and requirements, and show examples of key data products. It is important to note that geometric factors are averages over the entire calibration energy range.

11.1 Geometric Factor

Figure 48 demonstrates an important characteristic of HPCA response. Based on correlated TOF data, Fig. 48 illustrates the nearly uniform dependence of A_{eff}, $\langle \Delta\alpha \Delta E/E \rangle$, $\Delta\beta$ and geometric factor on energy. The slight variations in A_{eff} and $\langle \Delta\alpha \Delta E/E \rangle$ cause the slight variation in GF across the energy range.

As shown in Table 8 the four instruments have nearly identical responses with the exception of sensitivity. FM1 and FM2 have $\sim$50 % lower sensitivities (i.e., total GF, per pixel GF, and effective area) than FM3 and FM4. The differences, which are accounted for in additional calibration data not shown here, arise from setting the threshold for all four constant fraction discriminators at 2×10^7 electrons for the same MCP voltage. In retrospect

Table 8 Summary of calibration results at 3159 eV

Parameter	Requirement	FM1	FM2	FM3	FM4
Total geometric factor [cm^2 sr eV/eV]	3.0×10^{-3}	2.3×10^{-3}	2.5×10^{-3}	3.6×10^{-3}	3.6×10^{-3}
Pixel geometric factor [cm^2 sr eV/eV]	$\sim 2 \times 10^{-4}$	1.5×10^{-4}	1.5×10^{-4}	2.2×10^{-4}	2.3×10^{-4}
Effective aperture [cm^2 cts/ion]	$\sim 4 \times 10^{-2}$	3.8×10^{-2}	4.3×10^{-2}	7.2×10^{-2}	7.1×10^{-2}
Mass range [amu/q]	1 to 16	1 to 28	1 to 28	1 to 28	1 to 28
Mass resolution [$M/\Delta M$ FWHM]	4	>4	>4	>4	>4
Energy range [eV]	10 to 30,000	31 to 32,040	98 to 32,040	98 to 32,040	98 to 32,040
Energy resolution [$\Delta E/E$]	≤0.2	0.12 ± 0.01	0.10 ± 0.01	0.10 ± 0.01	0.096 ± 0.2
Analyzer constant	5.45 ± 0.1	5.45	5.45	5.39	5.40
Azimuth passband FWHM	$8° \pm 1.0°$	$7.6° \pm 0.3°$	$7.7° \pm 0.3°$	$7.1° \pm 0.4°$	$7.1° \pm 0.2°$
Elevation passband centers separation	$22.5° \pm 0.1°$	$22.6° \pm 0.2°$	$22.5° \pm 0.9°$	$22.5° \pm 0.3°$	$22.5° \pm 0.3°$
Elevation passband FWHM	$22.5° \pm 2.5°$	$24.0° \pm 0.7°$	$24.8° \pm 0.7°$	$23.1° \pm 0.7°$	$23.8° \pm 0.7°$
RF H^+ attenuation 0.5 to 2.5 keV	≥30×	>30	>30	>30	>30
RF H^+ attenuation $E \geq 2.5$ keV	≥8×	>8× @ 3.2 keV	>8× @ 3.2 keV	>8× @ 3.2 keV	>8× @ 3.2 keV
Singles dead time [μs]	≤1.0	0.2	0.2	0.7	0.8
Coincidence dead time [μs]	≤3.0	2.5	2.7	2.5	3.0

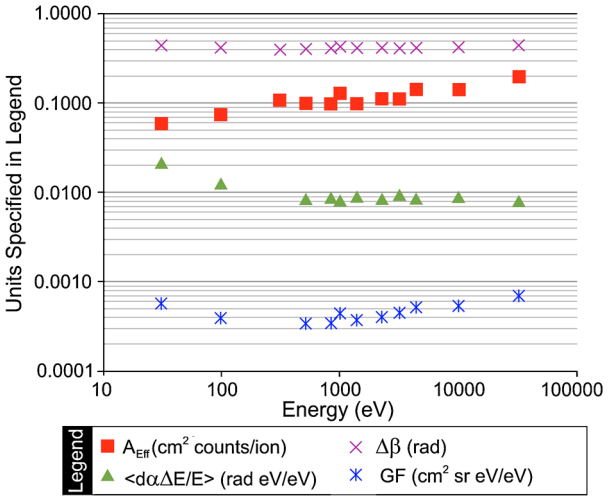

Fig. 48 Summation of calibration results as a function of energy over the full energy range. Data are from an HPCA FM1 start counter showing the dependence of four calibration parameters (GF, A_{eff}, $\Delta\beta$, and $\langle \Delta\alpha \Delta E/E \rangle$) on energy from 30 eV through 32 keV

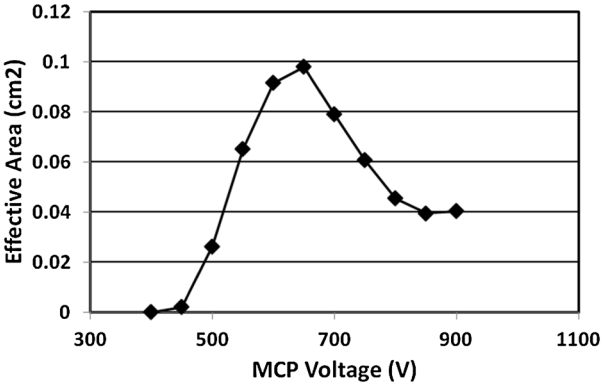

Fig. 49 Effective area of FM3 Anode 14 plotted against MCP voltage. The beam energy was 1.0 keV

this was not the best method for calibrating all four units because the MCPs in FM3 and FM4 were much "hotter", i.e., had much higher gain at a given voltage, than the FM1 and FM2 MCPs. As a consequence more pulses (counts) were recorded by the latter at a given ion beam current than by the former. Rather than repeating the lengthy calibration process for FM1 and FM2 we calibrated their response for different MCP gains at a constant beam current of 0.165 pA (shown for FM3 in Fig. 49). Comparable data was recorded for all 16 anodes on all four flight models and will be used to normalize sensitivity of the four units.

11.2 Mass Range and Resolution

Figure 20 shows a sample TOF spectrum at 3.159 keV plotted on a log scale to show that all species are separated at ~10 % of peak height, easily meeting the resolution requirement of $M/\Delta M = 4$ at FWHM. The areas marked in red delineate TOF channel boundaries used for ion species selection. It is also evident from Fig. 20 that although there is a noise floor that increases at low masses, the signal peak to noise ratio is always >10. Figure 31 shows measured TOF channel boundaries over the entire energy range.

Figure 50 is a comparison of TOF data and theory for 2.269 keV ions that should follow the TOF relationship given earlier in (18) and repeated here

$$T\ [\text{ns}] = 22.85L\ [\text{cm}]\big(M\ [\text{amu}]/E^*\ [\text{keV}]\big)^{1/2}. \tag{18}$$

Neglecting energy loss in the foil (ΔE_{foil}), from (17) the internal ion energy E^* is

$$E^* = E_0 + qV_{\text{acc}} = 2.269\ \text{keV} + 15.0\ \text{keV} = 17.269\ [\text{keV}]. \tag{44}$$

Using the central ray distance $L = L_0 = 3.15$ cm (see Fig. 19) then (18) gives

$$T = 71.98\ (M/17.260)^{1/2} = 17.32M^{1/2}\ [\text{ns}]. \tag{45}$$

Experimental data in Fig. 50 differ slightly from theory because of an offset of 7.27 ns in the flight model delay line. Calibrating out the offset by subtracting 7.27 ns makes the two fits nearly identical. The difference between the N^+ TOF peak at 85 ns for 1.0 keV ions (Fig. 23) vs. 75 ns here (including the TOF offset) is due to use of one amplifier per ring for data in Fig. 23 vs. flight configuration delay lines in Fig. 50. (Data in Fig. 23 could only be obtained with separate amplifiers—not the delay lines in flight configuration.)

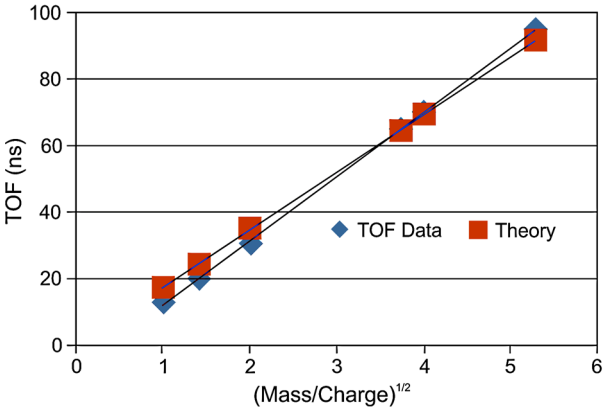

Fig. 50 Plot of ion TOF vs. $(M/q)^{1/2}$ for H^+, H_2^+, He^+, N^+, O^+, and N_2^+. Data were taken at the pre-programmed energy step of 2.269 keV

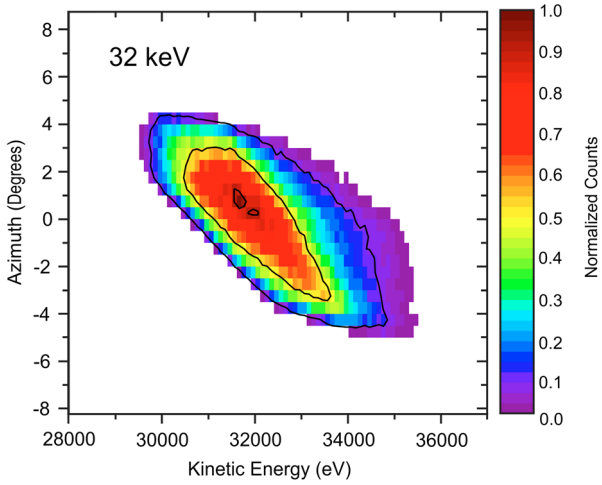

Fig. 51 Azimuthal angle vs. energy passband taken at 32 keV

11.3 Azimuth-Energy Passband

Examples of the coupled angle-energy response of the ESA passbands without RF applied were shown in Figs. 24a and 24c. Figure 51 is another energy-angle passband taken at a much higher energy (32 keV). Figure 52 shows individual azimuth, elevation and energy passbands along with simulations that agree well with data. Figure 53 is a series of 7 adjacent energy passbands showing their relative width and separation. Although the passbands are narrower than their separation, with this resolution the energy range is well sampled without any fear that an ambient plasma distribution might fall between the passbands. For that to happen the Mach number of the plasma flow would have to be much higher even than that of the solar wind.

11.4 Analyzer Constant

Comparison of the incident ion energy measured at every beam setting with the high resolution ESA micro-stepped voltage scans (Fig. 53) yields a very accurate measurement of the analyzer constant of 5.45 which is within expected error limits (Table 8).

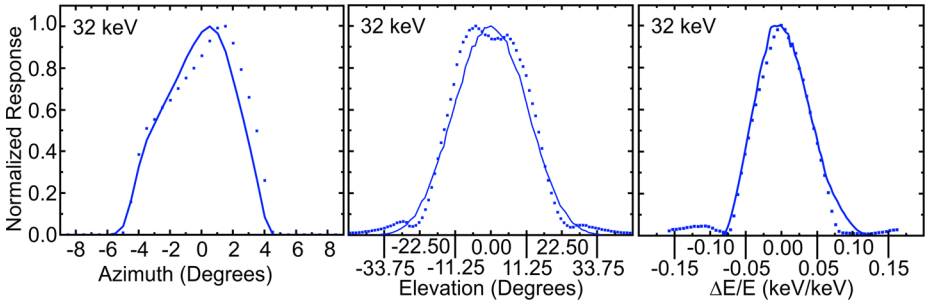

Fig. 52 Individual passbands summed over energy and angle using data from Fig. 51. *Dots* are data taken with the EPIC ion beam while *lines* are simulations

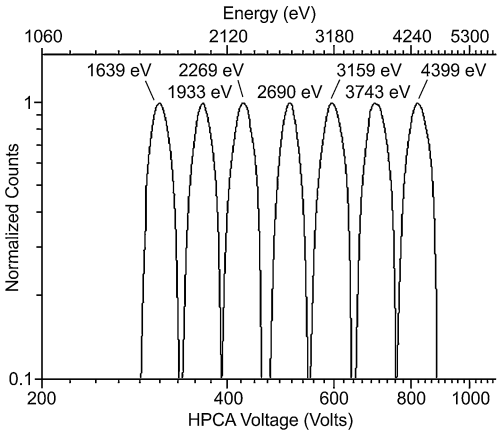

Fig. 53 Seven energy passbands covering center energies from 1639 to 4399 eV. The ratio of energy (*top scale*) to applied voltage on the ESA (*bottom scale*) gives an analyzer constant of 5.45

11.5 Elevation Passband

Figure 54 shows the 16 elevation passbands measured at 3.159 keV. The passbands overlap at about their half maximum points and are evenly spaced at 22.5°. The variation in amplitude by a factor of two across the passbands is a well known effect caused by a variation in MCP gain due to the unidirectional bias angle of the MCP's micro-channels. (Because of the channel bias of about 8° the gain depends on the incident angle of ions with respect to the channels and changes with position around the periphery of the MCP.)

11.6 RF Attenuation

During calibration the amount of attenuation as a function of RF settings was taken for all four species (H^+, H_2^+, He^+, N^+) at five energies out of the 14 within the RF operating range (Table 4). Figure 23 is an example of a family of attenuation curves for protons taken with the prototype at 1.0 keV (the approximate location of peak proton flux in Fig. 2). In Fig. 23 flux attenuation is plotted as normalized counting rate summed over proton TOF channels vs. peak-to-peak RF voltage for a range of frequencies. These data show that the requirement for proton attenuation >30 is easily achieved over the full range of frequencies (Table 8). Using calibration data of this type, a table of frequency vs. amplitude as a function of energy has been created that can be used to command any desired attenuation. In addition

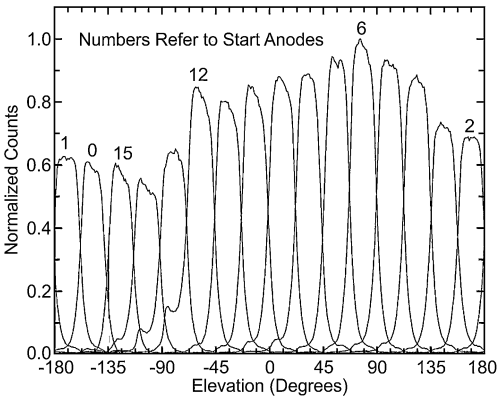

Fig. 54 Elevation passbands for each of 16 anodes. Counts are normalized to 1.0. Numbers above some of the passbands refer to start anodes which are referenced to the sensor structure

Table 9 HPCA allocated and measured resources for FM1

Resource	Allocation	Measurement
Fast Survey Power (W)	15.93	14.48
Slow Survey Power (W)	11.47	10.43
Mass (kg)	9.89	8.91

to total flux, the shapes of the passbands of attenuated fluxes are recorded (Fig. 24) allowing accurate reconstruction of velocity distributions.

As mentioned earlier, attenuation has an effect on the azimuth-energy passband (Fig. 24). The large reduction in transmitted flux at both energies in the figure is apparent from the color scale on the right. In addition to attenuating ion fluxes however, the RF field also shifts the main passbands to lower voltages by about 13 % and to lower azimuths by $-2°$. The shifts are caused by asymmetries in the ESA electric field introduced by the RF (refer back to trajectories in Fig. 9). Using this calibration information the small shifts in energy and FOV passbands can be taken into account during analysis. Figures 24c and 24d show similar responses for 3.159 keV, which is near the upper end of the RF operating range. As expected there is less attenuation than in the 0.995 keV case. However, by this point proton fluxes have fallen by roughly an order of magnitude. The RF also creates side lobes on the distributions (Figs. 24b and 24d) but they have negligible intensity and can be ignored or corrected in analysis.

11.7 Resources

Although technically not part of calibration, the instrument was weighed and its power consumption measured (Table 9). The difference between power consumption in the Fast and Slow Survey modes is the power required for the RF system, which is run only in the Fast mode.

12 Summary and Conclusions

HPCA is a novel instrument designed to meet the demanding measurement requirements of the MMS mission. The HPCA will contribute significantly to the definitive investigation of magnetic reconnection under all conditions wherever it might occur. Calibration has shown

that the HPCA optics, detector, electronics and software perform as required, allowing it to produce accurate results over the full range of operating conditions. Performance requirements presented in Table 2 are all met and, in particular, the requirement for high dynamic range so critical to successful measurements of minor species, is met with reserves. Calibration also demonstrates that the performance of all four units is very nearly the same. At this point all four flight models of the HPCA have been delivered and integrated on their respective spacecraft with one slight mismatch in the unit numbering scheme: FM 1 and 2 are on Observatories 1 and 2; FM 3 is on Observatory 4 and FM 4 on Observatory 3.

Acknowledgements Development of the HPCA has been an ongoing effort at SwRI for the past 10 years. We acknowledge generous support by the SwRI Internal Research program. We wish to thank members of the staff at SwRI, in particular W.C. Gibson and R.K. Black for their management skills directing the SwRI portions of the mission. We thank APL staff members and the APL internal research program for supporting development of the TOF ASICs and TOF board. At LMATC we particularly wish to thank Alex Price. We also acknowledge the support of members of the MMS project staff who helped with accommodating HPCA on the MMS spacecraft. HPCA was developed under NASA MMS contract NNG04EB99C. Work at APL was performed under SwRI subcontract 599789Q and at Lockheed Martin under SwRI subcontract 899039BT.

References

F. Allegrini, D.J. McComas, D.T. Young et al., Energy loss of 1–50 keV H, He, C, N, O, Ne and Ar ions transmitted through thin carbon foils. Rev. Sci. Instrum. **77**, 044501 (2006)

H. Balsiger, P. Eberhardt, J. Geiss, A. Ghielmetti, H.P. Walker, D.T. Young, H. Loidl, H. Rosenbauer, A satellite-borne ion mass spectrometer for the energy range 0 to 16 keV. Space Sci. Instrum. **2**, 499–521 (1976)

J.L. Burch et al., Magnetospheric multiscale overview and science objectives (2014, this volume)

J.L. Burch, G.P. Miller, A. De Los Santos, C.J. Pollock, S.E. Pope, P.W. Valek, D.T. Young, Technique for increasing the dynamic range of space-borne ion composition instruments. Rev. Sci. Instrum. **76**, 103301 (2005)

K. Byrum, H.J. Frisch, J.-F.C. Genat et al., Position sensing using pico-second timing with micro-channel plate devices and waveform sampling. IEEE Trans. Nucl. Sci. (2010). doi:10.1109/TNS.2009.2039805

G.A. Collison, J.C. Dorelli, L.A. Avranov et al., The geometric factor of electrostatic plasma analyzers: a case study from the fast plasma investigation for the magnetospheric multiscale mission. Rev. Sci. Instrum. **83**, 033303 (2012)

J.F. Drake, M. Swisdak, T.D. Phan et al., Ion heating resulting from pickup in magnetic reconnection exhausts. J. Geophys. Res. **114**, A05111 (2009). doi:10.1029/2008JA013701

M. Fränz, E. Dubinin, E. Roussos, J. Woch et al., Plasma moments in the environment of Mars: Mars express ASPERA-3 observations. Space Sci. Rev. **126**, 165–207 (2006)

S.A. Fuselier, W.S. Lewis, C. Schiff, R. Ergun, J.L. Burch, S.M. Petrinec, K.J. Trattner, Magnetospheric multiscale science mission profile and operations (2014, this volume)

J. Geiss, H. Balsiger, P. Eberhardt, H.P. Walker, L. Weber, D.T. Young, H. Rosenbauer, Dynamics of magnetospheric ion composition as observed by the GEOS mass spectrometer. Space Sci. Rev. **22**, 537–566 (1978)

G. Gloeckler, Ion composition measurement techniques for space plasmas. Rev. Sci. Instrum. **61**(11), 3613–3620 (1990)

R.G. Gomez, Simulation and optimization of ESA designs for space plasma missions. Ph.D. thesis, Rice University (2011). Publication Number: AAT 3463881; ISBN: 9781124772523

J.T. Gosling, M.F. Thomsen, R.C. Anderson, A cookbook for determining transmission characteristics of spherical section analyzers (1984). LANL Manual LA-10147-M

M. Hesse et al. (2014, this volume)

M.M. Kuznetsowa, M. Hesse, D. Winske, Collisionless reconnection supported by nongyrotropic pressure effects in hybrid and particle simulations. J. Geophys. Res. **106**(A3), 3799–3810 (2001)

D.J. McComas, J.E. Nordholt, D.T. Young, J.J. Berthelier, The Cassini mass spectrometer, in *Measurement Techniques in Space Plasmas: Particles*, ed. by R.F. Pfaff, J.E. Borovsky, D.T. Young. AGU Geophys. Monograph Ser., vol. 102, (1998), pp. 187–193

T.E. Moore, C.R. Chappell, M.O. Chandler, S.A. Fields, C.J. Pollock, D.L. Reasoner, D.T. Young, J.L. Burch, N. Eaker, J.H. Waite, D.J. McComas, J.E. Nordholt, M.F. Thomsen, J.J. Berthelier, R. Robson, The thermal ion dynamics experiment and plasma source instrument. Space Sci. Rev. **71**, 409–458 (1995)

N.P. Paschalidis, N. Stamatopoulos, K. Karadamoglou, G. Kottaras, V. Paschalidis, E. Sarris, R. McEntire, D. Mitchell, R. McNutt, A CMOS time of flight system on a chip for spacecraft instrumentation. IEEE Trans. Nucl. Sci. **49**, 1156–1163 (2002)

N. Paschalidis et al., Particle and photon imaging detector with 4-D output: absolute time-of-hit, X–Y position, and pulse height: application to space science particle instruments, IEEE Nuclear Science Symposium and Medical Imaging Conference, N02-53, Dresden, Germany (2008)

N.P. Paschalidis, D.T. Young, E. Donald, A. Jacques, A. DeLosSantos, J. Burch, R. Gomez, G. Miller, K. Pickens, C. Pollock, A delay line based time, position, and velocity determination system for a time of flight plasma spectrometer, in *38th COSPAR Scientific Assembly, Presentation D24-0047-10, Bremen, Germany* (2010)

G. Paschmann, I. Papamastorakis, W. Baumjohann, N. Sckopke, C.W. Carlson, B.U.O. Sonnerup, H. Lohr, The magnetopause for large magnetic shear: AMPTE/IRM observations. J. Geophys. Res. **91**(A10), 11,099–11,115 (1986)

T. Phan, H.U. Frey, S. Frey, L. Peticolas, S. Fuselier, C. Carlson, H. Reme, J.-M. Bosqued, A. Balogh, M. Dunlop, L. Kistler, C. Mouikis, I. Dandouras, J.-A. Sauvaud, S. Mende, J. McFadden, G. Parks, E. Moebius, B. Klecker, G. Paschmann, M. Fujimoto, S. Petrinec, M.F. Marcucci, A. Korth, R. Lundin, Simultaneous Cluster and IMAGE observations of cusp reconnection and auroral proton spot for northward IMF. J. Geophys. Res. Lett. **30**(10), 1509 (2003). doi:10.1029/2003GL016885

M.A. Shay, J.F. Drake, B.N. Rogers, R.E. Denton, Alfvenic collisionless magnetic reconnection and the Hall term. J. Geophys. Res. **106**(A5), 3759–3772 (2001)

M. Wuest, in *Measurement Techniques in Space Plasmas: Particles*, ed. by R.F. Pfaff, J.E. Borovsky, D.T. Young. AGU Geophys. Monograph Ser., vol. 102 (1998), pp. 141–155

M. Wuest, D.S. Evans, J.P. McFadden, W.T. Kasprzak, L.H. Brace, B.K. Dichter, W.R. Hoegy, A.J. Lazarus, A. Masson, O. Vaisberg (International Space Science Institute), in *Calibration of Particle Instruments in Space Physics* (2007), pp. 11–116

D.T. Young, H. Balsiger, J. Geiss, Correlations of magnetospheric ion composition with geomagnetic and solar activity. J. Geophys. Res. **87**, 9077–9096 (1982)

D.T. Young, S.J. Bame, M.F. Thomsen, R.H. Martin, J.L. Burch, J.A. Marshall, B. Reinhard, 2π-radian field-of-view toroidal electrostatic analyzer. Rev. Sci. Instrum. **59**, 743–751 (1988)

D.T. Young, Space plasma mass spectrometry below 60 keV, in *Solar System Plasma Physics*, ed. by J.H. Waite Jr., J.L. Burch, R.L. Moore. Geophys. Monograph Ser., vol. 54 (1989), pp. 143–157

D.T. Young, J.A. Marshall, J.L. Burch, S.J. Bame, R.H. Martin, A 360° field-of-view toroidal ion composition analyzer using time-of-flight, in *Solar System Plasma Physics*, ed. by J.H. Waite Jr., J.L. Burch, R.L. Moore. Geophys. Monograph Ser., vol. 54 (1989), pp. 171–176

D.T. Young et al. (1990)

D.T. Young, J.J. Berthelier, M. Blanc, J.L. Burch, A.J. Coates, R. Goldstein, M. Grande, T.W. Hill, R.E. Johnson, V. Kelha, D.J. McComas, E.C. Sittler, K.R. Svenes, K. Szegö, P. Tanskanen, K. Ahola, D. Anderson, S. Bakshi, R.A. Baragiola, B.L. Barraclough, R.K. Black, S. Bolton, T. Booker, R. Bowman, P. Casey, G. Dirks, N. Eaker, J.T. Gosling, H. Hannula, C. Holmlund, H. Huomo, J.M. Illiano, P. Jensen, M.A. Johnson, D. Linder, T. Luntama, S. Mayrice, K. McCabe, B.T. Narheim, J.E. Nordholt, A. Preece, J. Rudzki, A. Ruitberg, K. Smith, S. Szalai, M.F. Thomsen, K. Viherkanto, T. Vollmer, T.E. Wahl, M. Wuest, T. Ylikorpi, C. Zinsmeyer, Cassini plasma spectrometer investigation. Space Sci. Rev. **114**, 1–112 (2004)

D.T. Young, J.E. Nordholt, J.L. Burch, D.J. McComas, R.P. Bowman, R.A. Abeyta, J. Alexander, J. Baldonado, P. Barker, R.K. Black, T.L. Booker, P.J. Casey, L. Cope, F.J. Crary, J.P. Cravens, H.O. Funsten, R. Goldstein, D.R. Guerrero, S.F. Hahn, J.J. Hanley, B.P. Henneke, E.F. Horton, D.J. Lawrence, K.P. McCabe, D. Reisenfeld, R.P. Salazar, M. Shappirio, S.A. Storms, C. Urdiales, J.H. Waite Jr., Plasma experiment for planetary exploration. Space Sci. Rev. **129**, 327–357 (2007)